The G^0 Experiment
Backward Angle Measurements

The G^0 Collaboration

California Institute of Technology, Carnegie-Mellon University, College of William and Mary, Hampton University, L'Institut de Physique Nucléaire d'Orsay, L'Institut des Sciences Nucléaires de Grenoble, Louisiana Tech. University, New Mexico State University, Thomas Jefferson National Laboratory, TRIUMF, University of Connecticut, University of Illinois at Urbana-Champaign, University of Kentucky, University of Manitoba, University of Maryland, University of Massachusetts, University of Northern British Columbia, Virginia Tech, and Yerevan Physics Institute

May 2001

Contents

1 Summary

This submission regarding the G^0 experiment has been prepared for consideration by the Jefferson Lab Program Advisory Committee at its PAC20 meeting. The G^0 experiment has been approved previously at three PAC meetings (as 91-017 in December 1993, 99-016 in January 99 and 00-006 in January 00); these approvals have covered the experiment commissioning and the forward angle running. In this proposal we request 70 calendar days of running the first kinematic point (30 days each for hydrogen and deuterium targets plus 10 days for commissioning) of the backward angle segment of the experiment.

In the G^0 experiment, parity-violating asymmetries in elastic electron scattering from the nucleon will be measured at both forward and backward angles and over a range of momentum transfers from about 0.1 – 1.0 GeV^2/c^2. The primary purpose of the experiment is to separate the s quark contributions ($G_E^s(Q^2)$ and $G_M^s(Q^2)$) to the overall charge and magnetization densities of the nucleon using these measurements. No other existing or proposed experiment will perform the separation directly over this range of momentum transfers. At backward angles we will measure quasi-elastic scattering from a deuterium target to extract the nucleon anapole form factor (sometimes referred to as "radiative correction") contributions (included in $G_A^e(T=1)$) to these asymmetries. The recent report of this contribution by the SAMPLE collaboration suggests that this form factor may be larger than expected. *The backward angle measurements proposed herein, in concert with the forward angle measurement already approved, are necessary to separate these form factors.* Running with a deuterium target necessitates particle identification measurements for which we propose adding a Cerenkov counter, to be discussed in detail in Sections 3.3 and 4.1.3. Otherwise, especially in terms of false asymmetries, the forward and backward angle measurements are essentially the same (asymmetries are larger in the backward direction). At the backward angles we will also measure the axial vector N-Δ transition form factor (a separate proposal has been submitted for this experiment; the relevant technical sections of the two proposals are the same). A special purpose, superconducting toroidal spectrometer with large, azimuthally symmetric angular acceptance and an associated cryogenic target have been constructed for these measurements.

A great deal of progress has been made by the 19 institutions (see Table 1.1) involved in the project over the past 18 months. A summary of these activities is included in the Appendix in the form of a copy of the progress report for our annual DOE/NSF review (June 6/7, 2001). Since PAC17 many aspects of the experiment have moved from the construction and assembly stages to the testing stages. We are presently in the "chain testing" stage wherein two octants of detectors - one each of North American (NA) and French - placed in Hall C, are being checked out through the electronics and DAQ systems to analysis software. Some other important areas of progress include:

- development and initial tests of a prototype laser for high bunch charge, high polarization operation of the electron source,

- delivery to Illinois and initiation of testing of the superconducting spectrometer magnet,
- completion of the magnetic field measurement gantry for the magnet
- delivery to JLab and beginning of testing of the liquid hydrogen/deuterium target,
- completion of assembly and initial testing of 4 North American (NA) detector octants; "installation" of one octant in Hall C
- completion of the detector gain monitoring system
- completion of assembly and initial testing of three French detector octants (final octant to be delivered in August 01); "installation" of one octant in Hall C
- completion of fabrication and individual module testing of all NA custom electronics (modulo last items of mean timer module production); partial delivery to JLab beginning of chain testing (remaining modules to JLab for September 01 installation),
- completion and partial delivery of integrated French electronics modules (remaining modules to JLab for September 01 installation)
- beginning of fabrication of cryostat exit detectors
- standard GEANT simulation package, development of DAQ, slow controls and analysis software
- initial hardware/software DAQ test setup run in Summer 2000; final system assembled for chain test
- completion of detector support, completion of cabling to Hall, installation of cryogen feed lines and reservoir, installation of detector rails

The cost and schedule for the experiment as established in the G^0 Management Plan are holding. Subsequent to PAC17, the status of the experiment was favorably reviewed by the NSF/DOE Review (Barish) Committee (June 2000, submission and report included in the PAC20 package). At the time of writing about \$4.0M of the \$5.6M construction project has been committed (not including contingency); the remaining expenditures are mostly associated with installation. The available contingency for the remaining work is at about 36% across the project. Two installation periods have been identified by the laboratory - September '01 in the firm schedule for installation of the detector octants into their support and February - May '02 in the tentative schedule for installation of the magnet and target.

With this submission, we propose that the backward angle measurements of the G0 experiment include three momentum transfers (Q^2 = 0.3, 0.5 and 0.8 GeV^2) to provide reasonable information on the Q^2 dependence of G_E^s, G_M^s and $G_A^e(T=1)$ within the range accessible to the experiment. *At this time* we request that the PAC approve 70 d (30 d each for measurements with hydrogen and deuterium targets at $Q^2 = 0.8$ GeV^2 as well as 10 d for commissioning the back angle setup) of beam time for the backward angle asymmetry measurement. This time will provide the first back angle asymmetry to match the range of our forward angle measurements, and with the deuterium measurement allow us to determine G_E^s, G_M^s and $G_A^e(T=1)$. The highest Q^2 point has been chosen for the first measurement because it is the least problematic from the point of view of the accelerator (incident energy of 0.799 GeV). We note that the time requested here for the back angle running is based on a rough equalization of contributions from the forward and backward angle asymmetries to the overall uncertainty in these quantities (see Section 6.1).

California Institute of Technology				
R. Carr	S. D. Corvig	B. Filippone	K. Gustafsson	L. Hannelius
T. M. Ito	J. Martin	R. D. McKeown†		
Carnegie-Mellon University				
R. Clark	G. Franklin	J. Lachniet	R. McCrady	C. Meyer
B. Quinn†	R. A. Schumacher			
College of William and Mary				
D. S. Armstrong†	T. D. Averett	J. M. Finn	K. A. Griffioen	J. Roche
J. Secrest				
Hampton University				
K. McFarlane†				
IPN Orsay				
J. Arvieux†	L. Bimbot	R. Frascaria	X. Grave	D. Marchand
P. Rosier	R. Sellem	J. van de Wiele		
ISN Grenoble				
G. Batigne	C. Furget	S. Kox†	G. Quemener	J. Real
R. Tieulent	E. Voutier			
Louisiana Tech. Univ.				
K. Johnston†	N. Simicevic	S. Wells		
New Mexico State University				
D. McKee	M. Nakos	V. Papavassiliou†	S. Pate†	
TJNAF				
P. Brindza	R. D. Carlini†	H. Fenker	A. Lung†	D. J. Mack
G. Smith	W. F. Vulcan	S. A. Wood	C. Yan	
TRIUMF				
C. A. Davis†	T. Ries			
University of Connecticut				
M. J. Ramsey-Musolf†				
University of Illinois				
D. H. Beck†	R. D. Hasty	P. Kammel	K. Nakahara	A. M. Nathan
G. Selvaggi	D. T. Spayde	S. Williamson†		
University of Kentucky				
D. Dale	W. Korsch†	V. Zeps		
University of Manitoba				
J. Birchall	W. R. Falk	L. Lee	S. A. Page	W. D. Ramsay
A. W. Rauf	G. A. Rutledge	W. T. H. van Oers†		
University of Maryland				
E. J. Beise†	H. Breuer	N. Chant	A. Cowley	P. M. King
J. LeNoble	J. Liu	R. Neveling	P. Roos	
University of Massachusetts				
B. R. Holstein†				
University of Northern British Columbia				
E. Korkmaz†	T. Porcelli			
Virginia Tech				
A. Hawthorne Allen	M. L. Pitt†	J. Yun		
Yerevan Physics Institute				
R. Asaturyan	H. Mkrtchyan†	S. Stepanyan	V. Tadevosyan	

Table 1.1: Active participants in the G^0 backward angle measurements († indicates contact person).

In this proposal we provide a discussion of the back angle elastic scattering experiment, descriptions of the detectors and electronics to be used (including the new Cerenkov detector) and conclude with a discussion of management, funding, schedule and the beam time request.

2 Physics

The parity-violating interaction between electrons and nucleons primarily involves interference between the dominant electromagnetic (γ exchange) and the exchange of a Z boson. Due to the parity-violating nature of the weak interaction, these interference effects imply the existence of small pseudoscalar observables in electron scattering experiments. Much of the discussion in this section is elaborated upon in the review article [1] by D. Beck and R. McKeown.

One generally measures the ratio of helicity dependent to helicity independent cross sections, or the parity-violating asymmetry:

$$A = \frac{d\sigma_R - d\sigma_L}{d\sigma_R + d\sigma_L} \tag{2.1}$$

where σ_R and σ_L are the cross sections for right- and left-handed electrons, respectively. This quantity will generally be proportional to a product of neutral weak couplings $v^Z \cdot a^Z$ that contains the physics of interest. Thus, measurement of the helicity dependence in elastic electron-proton scattering can be used to study the neutral weak vector form factors of the nucleon [2, 3, 4]. There is also sensitivity to the weak axial vector form factors; these are suppressed at leading order but are also of great interest and should be measured.

The parity-violating asymmetry for elastic electron-proton scattering is given by the following expression [5]:

$$A = \left[\frac{-G_F Q^2}{4\sqrt{2}\pi\alpha}\right] \frac{\varepsilon G_E^\gamma G_E^Z + \tau G_M^\gamma G_M^Z - (1-4\sin^2\theta_W)\varepsilon' G_M^\gamma G_A^e}{\varepsilon (G_E^\gamma)^2 + \tau (G_M)^2} \tag{2.2}$$

$$\equiv -\frac{G_F Q^2}{4\sqrt{2}\pi\alpha} \times \frac{\mathcal{N}}{\mathcal{D}} \tag{2.3}$$

where

$$\begin{aligned} \tau &= \frac{Q^2}{4M_N^2} \\ \varepsilon &= \frac{1}{1+2(1+\tau)\tan^2\frac{\theta}{2}} \\ \varepsilon' &= \sqrt{\tau(1+\tau)(1-\varepsilon^2)} \end{aligned} \tag{2.4}$$

are kinematic quantities, $Q^2 > 0$ is the four-momentum transfer, and θ is the laboratory electron scattering angle.

The quantities G_E^γ, G_M^γ, G_E^Z, and G_M^Z are the vector form factors of the nucleon associated with γ- and Z-exchange. The electromagnetic and weak form factors are (in lowest order) related via the flavor dependence of the fundamental Z-q couplings. The flavor structure of these form factors and the radiative corrections are considered in more detail below.

The neutral weak e-N interaction also involves an axial vector coupling G_A^e in the third term of the numerator in Eqn.(2.2). The tree-level Z-exchange process is responsible for the $1-4\sin^2\theta_W$ factor that appears in this expression and, as noted in [5, 6], higher order processes can contribute significantly. These include interesting anapole effects and other electroweak radiative corrections as discussed below.

It is important to note that the three terms in the numerator can be separately determined via a series of measurements. At very small scattering angles, the G_E term is dominant due to the large value of ϵ. This is the focus of the forward angle measurements already planned for G0. At larger scattering angles, one is sensitive to a combination of both the G_M^Z term and the G_A^e (axial) term. Although one expects the G_M^Z term to be dominant, the axial term can not be neglected, and indeed it is of great interest to study this term as well. Separation of these terms via kinematic measurements on the proton is extremely difficult. The best method to separate the magnetic and axial terms is to utilize quasielastic scattering from deuterium.

For a nucleus with Z protons and N neutrons the quasielastic asymmetry can be written in the simple form (ignoring final state interactions and other nuclear corrections):

$$A_{\rm nuc} = -\frac{G_F Q^2}{4\sqrt{2}\pi\alpha} \times \frac{N\mathcal{N}_n + Z\mathcal{N}_p}{N\mathcal{D}_n + Z\mathcal{D}_p} \tag{2.5}$$

where $\mathcal{N}_p$ ($\mathcal{N}_n$) is the numerator expression and $\mathcal{D}_p$ ($\mathcal{D}_n$) the denominator (from Eqns. 2.2 and 2.3) for the proton (neutron), respectively. Effects associated with the deuteron wavefunction and different potential models have been explored in [7] and shown to be quite small. Of course, the corrections for final state interactions and exchange currents must be computed to enable reliable separation of the axial and magnetic form factors. Some of these issues have been addressed in recent work [8], and further work is in progress [9].

In order to determine G_E^s, G_M^s, and G_A^e at each Q^2 it is necessary to perform at least 3 independent measurements at each Q^2. The G0 program is a unique opportunity to perform a series of such measurements: a forward angle measurement on the proton (mostly sensitive to G_e^s), a backward angle measurement on the proton, and also a backward angle measurement of the quasielastic deuteron asymmetry.

2.1 Nucleon Vector Form Factors and Strangeness Content

The standard electroweak model couplings to the up, down, and strange quarks imply that the electromagnetic current operator has the simple familiar form

$$\hat{V}_\gamma^\mu = \frac{2}{3}\bar{u}\gamma^\mu u - \frac{1}{3}\bar{d}\gamma^\mu d - \frac{1}{3}\bar{s}\gamma^\mu s\,. \tag{2.6}$$

Similarly, the neutral weak vector current operator is given by the expression

$$\hat{V}_Z^\mu = (1-\frac{8}{3}\sin^2\theta_W)\bar{u}\gamma^\mu u + (-1+\frac{4}{3}\sin^2\theta_W)\bar{d}\gamma^\mu d + (-1+\frac{4}{3}\sin^2\theta_W)\bar{s}\gamma^\mu s\,. \tag{2.7}$$

Here the coefficients depend on the weak mixing angle, which is very accurately known ($\sin^2\theta_W = 0.23117 \pm 0.00016$ [10]). The flavor structure contained in these expressions forms the basis for a program to measure the flavor composition of the vector form factors. The measurements involve matrix elements of these operators (the form factors) which will reflect the underlying flavor dependence of these operators.

The electromagnetic form factors of the nucleon arise from matrix elements of the EM current operator

$$< N|\hat{V}_\gamma^\mu|N > \equiv \bar{u}_N\left[F_1^\gamma(q^2)\gamma^\mu + \frac{i}{2M_N}F_2^\gamma(q^2)\sigma^{\mu\nu}q_\nu\right]u_N \tag{2.8}$$

where $F_1^\gamma(q^2)$ and $F_2^\gamma(q^2)$ are the Dirac and Pauli electromagnetic form factors, which are functions of the squared momentum transfer. We will also use the Sachs form factors, which are linear combinations of the Dirac and Pauli form factors

$$\begin{aligned} G_E &= F_1 - \tau F_2 \\ G_M &= F_1 + F_2 \end{aligned} \tag{2.9}$$

where $\tau \equiv -q^2/4M_N^2 > 0$.

The quark flavor structure of these form factors can be revealed by writing the matrix elements of individual quark currents in terms of form factors:

$$< N|\bar{q}^j\gamma^\mu q^j|N > \equiv \bar{u}_N\left[F_1^j(q^2)\gamma^\mu + \frac{i}{2M_N}F_2^j(q^2)\sigma^{\mu\nu}q_\nu\right]u_N \tag{2.10}$$

where $j = u, d$, or s; this defines the form factors F_1^j and F_2^j. Then using definitions analogous to Eqn. (2.9), we can write

$$G_E^\gamma = \frac{2}{3}G_E^u - \frac{1}{3}G_E^d - \frac{1}{3}G_E^s \tag{2.11}$$

$$G_M^\gamma = \frac{2}{3}G_M^u - \frac{1}{3}G_M^d - \frac{1}{3}G_M^s \ . \tag{2.12}$$

In direct analogy to Eqn. (2.7), we have expressions for the neutral weak form factors G_E^Z and G_M^Z in terms of the different quark flavor components:

$$G_{E,M}^Z = (1 - \frac{8}{3}\sin^2\theta_W)G_{E,M}^u + (-1 + \frac{4}{3}\sin^2\theta_W)G_{E,M}^d + (-1 + \frac{4}{3}\sin^2\theta_W)G_{E,M}^s \ . \tag{2.13}$$

Again it is important to emphasize that the form factors $G_{E,M}^{u,d,s}$ appearing in this expression are *exactly* the same as those in the electromagnetic form factors in Eqns. (2.11, 2.12).

Utilizing charge symmetry, one then can eliminate the up and down quark contributions to the neutral weak form factors by using the proton and neutron electromagnetic form factors and obtain the expressions

$$G_{E,M}^{Z,p} = (1 - 4\sin^2\theta_W)G_{E,M}^{\gamma,p} - G_{E,M}^{\gamma,n} - G_{E,M}^s \ . \tag{2.14}$$

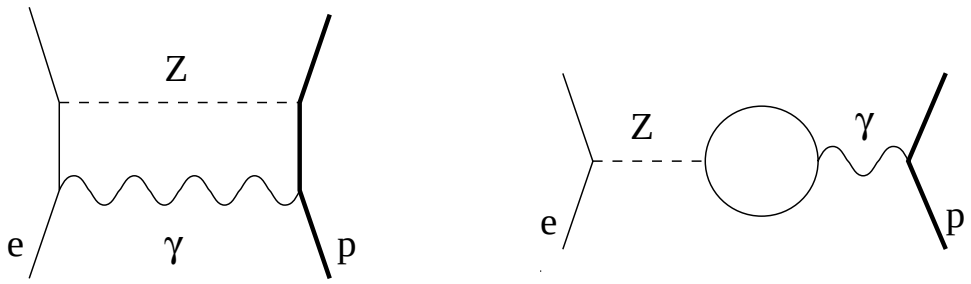

Figure 2.1: Examples of amplitudes contributing to electroweak radiative corrections ("$\gamma - Z$ box" on the left) and anapole corrections ("$\gamma - Z$ mixing" on the right).

This is a key result. It shows how the neutral weak form factors are related to the electromagnetic form factors plus a contribution from the strange (electric or magnetic) form factor. Thus measurement of the neutral weak form factor will allow (after combination with the electromagnetic form factors) determination of the strange form factor of interest.

The electromagnetic form factors present in Eqns. (2.11,2.12) are very accurately known (1-2 %) for the proton in the momentum transfer region $Q^2 < 1$ (GeV/c)^2. The neutron form factors are not known as accurately as the proton form factors (the electric form factor G_E^n is at present rather poorly constrained by experiment), although considerable work to improve our knowledge of these quantities is in progress. Thus, the present lack of knowledge of the neutron form factors will not significantly hinder the interpretation of the neutral weak form factors.

In obtaining Eqn. (2.14), it was assumed that charge symmetry was exact. Electromagnetic and quark mass effects can cause small violations of charge symmetry and introduce corrections to this relation. The effects of charge symmetry violation on the extraction of strange form factors from neutral weak and electromagnetic form factors has been treated in some detail in [11]. In that work it is found that these corrections are very small, generally less that about 1% of the electromagnetic form factors, and have only a minor effect the extraction of the strange form factors.

As mentioned above, there are electroweak radiative corrections to the coefficients in Eqn. (2.14) due to processes such as those shown in Figure 2.1. The above expressions for the neutral weak vector form factors $G_{p,n}^Z$ in terms of the electromagnetic form factors $G_{p,n}^\gamma$ are modified according to

$$G_{E,M}^{Z,p} = (1 - 4\sin^2\theta_W)(1 + R_V^p)G_{E,M}^{\gamma,p} - (1 + R_V^n)G_{E,M}^{\gamma,n} - G_{E,M}^s \; . \tag{2.15}$$

The correction factors have been computed [12, 6, 5] to be

$$\begin{aligned} R_V^p &= -0.054 \pm 0.033 \\ R_V^n &= -0.0143 \pm 0.0004. \end{aligned} \tag{2.16}$$

The properties of the strange form factors G_E^s and G_M^s near $Q^2 = 0$ are of particular interest in that they represent static properties of the nucleon. Thus it is customary to

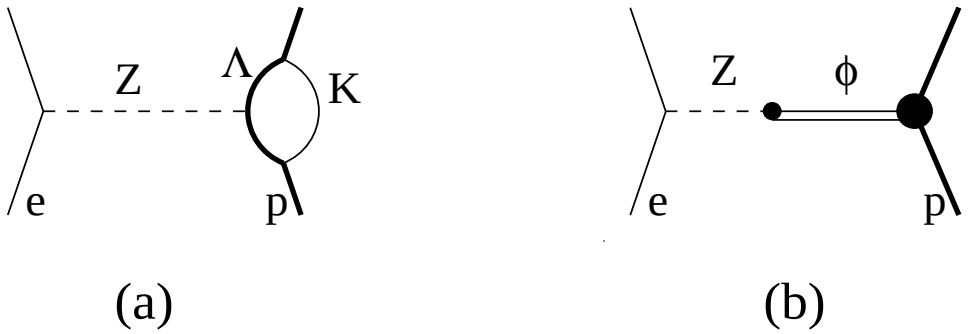

Figure 2.2: Examples of (a) loop and (b) pole diagrams used to compute strangeness effects in the nucleon.

define the quantity

$$\mu_s \equiv G_M^s(Q^2 = 0) \tag{2.17}$$

as the strange magnetic moment of the nucleon. Since the nucleon has no net strangeness, we find $G_E^s(Q^2 = 0) = 0$. However, one can express the slope of G_E^s at $Q^2 = 0$ in the usual fashion in terms of a "strangeness radius" r_s

$$r_s^2 \equiv -6 \left[dG_E^s/dQ^2 \right]_{Q^2=0} . \tag{2.18}$$

A variety of theoretical methods have been employed in efforts to compute the form factors $G_{E,M}^s(Q^2)$ (or often just the quantities μ_s and r_s). Figure 2.2 shows two examples of physical processes that may contribute. These are generically known as "loop" effects and "pole" effects. The loop effects [13, 14, 15, 16, 17] correspond to the fluctuation of the nucleon into a K-meson and hyperon. The physical separation of the s and $\bar{s}$ in such processes (or the production of $s\bar{s}$ in a spin singlet) leads to non-zero values of $G_{E,M}^s(Q^2)$. The pole processes [19, 20, 21] are associated with the fluctuation of the virtual boson (photon or Z) into a ϕ meson, which is predominantly an $\bar{s}s$ pair. Some attempts have been made to combine the two approaches using dispersion theoretical analyses [22]. Other models employ SU(3) extensions of the Skyrme model [23, 24, 25, 26] or the Nambu-Jona-Lasinio model. [29] Excited hyperons and strange mesons are also included in some treatments, and these contributions seem to be numerically significant. [17, 18] A detailed review of the various calculations can be found in Ref. [30].

A reasonably complete compilation of theoretical results for μ_s and r_s^2 is listed in Table 2.1. The calculated values of r_s^2 are small and there is no general agreement on the sign. However, there is evidently a trend in Table 2.1 that one should expect $\mu_s < 0$, generally in the range $-0.8 \rightarrow 0.0$ nuclear magnetons. Notable exceptions are references [24] and [26] which analyze the set of baryon magnetic moments in the context of a SU(3) generalization of the Skyrme model Hamiltonian.

2.2 Anapole form factor

As noted above, the parity-violating interaction of electrons with nucleons involves an axial vector coupling to the nucleon, G_A^e. This term in the parity-violating asymmetry contains

Table 2.1: Theoretical predictions for $\mu_s \equiv G_M^s(Q^2=0)$ and r_s^2.

Type of calculation	μ_s (n.m.)	r_s^2(fm^2)	Reference
Poles	-0.31 ± 0.09	$0.11 \to 0.22$	[19]
Kaon Loops	$-0.31 \to -0.40$	$-0.032 \to -0.027$	[13]
Kaon Loops	-0.026	-0.01	[14]
Kaon Loops	$\lvert\mu_s\rvert = 0.8$		[15]
SU(3) Skyrme (broken)	-0.13	-0.10	[23]
SU(3) Skyrme (symmetric)	-0.33	-0.19	[23]
SU(3) chiral hyperbag	$+0.42$		[24]
SU(3) chiral color dielectric	$-0.20 \to -0.026$	-0.003 ± 0.002	[31]
SU(3) chiral soliton	-0.45	-0.35	[25]
Poles	-0.24 ± 0.03	0.19 ± 0.03	[20]
Kaon Loops	$-0.125 \to -0.146$	$-0.022 \to -0.019$	[16]
NJL soliton	$-0.05 \to +0.25$	$-0.25 \to -0.15$	[29]
QCD equalities	-0.75 ± 0.30		[32]
Loops	$+0.035$	-0.04	[17]
Loops	-0.06	$+0.02$	[18]
Dispersion	$-0.10 \to -0.14$	$0.21 \to 0.27$	[22]
Chiral models	$-0.25, -0.09$	0.24	[33]
Poles	0.003	0.002	[21]
SU(3) Skyrme (broken)	$+0.36$		[26]
Lattice (quenched)	-0.36 ± 0.20	$-0.06 \to -0.16$	[27]
Lattice (chiral)	-0.16 ± 0.18		[28]

several effects beyond the leading order Z- exchange which can only be differentiated in theoretical calculations. Nevertheless, it is important to establish that the *experimentally observable* quantities are well-defined and unambiguous.

In parity-violating electron scattering the neutral weak axial form factor corresponding to tree-level Z-exchange is multiplied by the coefficient $1 - 4\sin^2\theta_W \ll 1$. This suppression of the leading amplitude increases the importance of anapole effects and other electroweak radiative corrections:

$$G_A^e = G_A^Z + \eta F_A + R_e \tag{2.19}$$

where

$$\eta = \frac{8\pi\sqrt{2}\alpha}{1 - 4\sin^2\theta_W} = 3.45, \tag{2.20}$$

$G_A^Z = G_A\tau_3 + \Delta s$, F_A is the nucleon anapole form factor (defined below), and R_e are radiative corrections. The normalization of $G_A\tau_3$ is obtained from neutron beta decay and its Q^2 dependence from charged current neutrino scattering; Δs is estimated from spin dependent deep inelastic scattering. G_A^Z is therefore completely determined by experiments independent of the present one. Typical contributions to R_e and F_A are shown in Figure 2.1. As discussed in [5, 6], the separation of F_A and R_e is actually a theoretical issue and dependent upon the choice of gauge. In calculations performed to date [12, 34] the anapole type effects associated with the "$\gamma - Z$ mixing" amplitudes are, in fact, the dominant

correction. We thus refer to the observable difference between G_A^e and G_A^Z as an anapole contribution, with the caveat that the complete set of radiative corrections must be included in any consistent quantitative theoretical treatment of G_A^e.

The anapole moment has been traditionally defined as the effective parity-violating coupling between real photons and nucleons [35]. (In practice, this quantity is only observable at finite momentum transfer associated with the parity-violating interaction between electrons and nucleons.) It appears as an additional term in Eqn. (2.8) when one includes the possibility that parity is not strictly conserved [34]:

$$\begin{aligned} \langle N|\hat{V}_\gamma^\mu|N\rangle &\equiv \bar{u}_N(p')\{F_1\gamma^\mu + \frac{i}{2M_N}F_2\sigma^{\mu\nu}q_\nu \\ &+ F_A\left[G_F(q^2\gamma^\mu - q^\nu\gamma_\nu q^\mu)\gamma^5\right]\}u(p) \end{aligned} \tag{2.21}$$

Note that our definition of F_A differs from that used in the atomic physics literature by a factor of $M_N^2 G_F$ with the result that the natural scale of F_A is of order unity. Thus, F_A could indeed provide a substantial contribution to G_A^e (see Eqn. (2.19)).

2.2.1 Theory Of The Anapole Contribution

As mentioned above, aside from the leading Z exchange term (G_A^Z) the dominant calculated contribution to G_A^e arises from the "$\gamma - Z$ mixing" diagram shown in Figure 2.1 [12, 34]. It should be noted that the evaluation of this amplitude ignores the strong interaction of the nucleon with the quark loop and so may not be numerically accurate. More recently, consideration of additional strong interaction effects associated with mesonic processes have indicated only relatively small additional corrections [38, 39, 40, 41]. It is important to note that the Q^2 dependence of the anapole form factor F_A could be different from the dipole form that is successful in fitting the tree level term G_A^Z. Maekawa and van Kolck [40] find to leading order in chiral perturbation theory that the momentum dependence of the anapole form factor is softer than the dipole form. Thus, it is important to measure this quantity over a range of Q^2 values. [40] The study of the anapole contributions and other corrections to G_A^e is presently an active area of experimental and theoretical investigation.

2.3 Previous experiments

The SAMPLE experiment at the Bates Linear Accelerator Center was the first to study strange form factors and the anapole contribution in parity-violating electron scattering. This experiment measures the elastic asymmetry from the proton and the quasielastic asymmetry from the deuteron at $Q^2 = 0.1$ GeV^2 [42, 43, 44, 45, 46]. In the most recent publication [47], analysis of the SAMPLE results is presented which yields values of the magnetic and axial form factors

$$G_M^s(Q^2 = 0.1) = +0.14 \pm 0.29 \pm 0.31\,, \tag{2.22}$$

$$G_A^e(T = 1) = +0.22 \pm 0.45 \pm 0.39. \tag{2.23}$$

These are both somewhat surprising, and have generated a great deal of interest. The value of G_M^s was generally expected to be negative, based on the theoretical calculations

(see Table 2.1). A recent theoretical study [48] of the Q^2 dependence of G_M^s predicts positive slope, in which case the SAMPLE result may actually indicate that $\mu_s \simeq 0$. Theoretical expectations for the axial form factor were $G_A^e(T=1) = -0.83 \pm 0.26$ [38] also in disagreement with the SAMPLE measurements. These results indicate that it is essential to study the axial form factor to extract reliable values of G_M^s, and of course G_A^e itself is quite interesting to experimentally study.

The HAPPEX experiment [50, 51] utilized the two spectrometers in Hall A at Jefferson Lab to measure parity violation in elastic electron scattering at very forward angles. The measured asymmetry, including the results from both phases of the experiment is

$$A_p(Q^2 = 0.477\text{GeV}^2,\, \theta_{av} = 12.3^\circ) = -14.60 \pm 0.94 \pm 0.54 \text{ ppm}\,. \tag{2.24}$$

This result has been interpreted (using an assumed value of G_A^e extrapolated from calculated $Q^2 = 0$ values) to yield the strange form factor combination

$$\frac{G_E^s + 0.392 G_M^s}{G_M^p/\mu_p} = 0.091 \pm 0.054 \pm 0.039\,. \tag{2.25}$$

While the results of the HAPPEX experiment exhibit small statistical uncertainties, it is difficult to draw firm conclusions from this single measurement. It appears that there is no strong evidence for the presence of strange quark effects, however, interpretation of these data is hindered by the dependence of the one measured asymmetry on three form factors. At these kinematics, the asymmetry depends on a linear combination of the strange electric and magnetic form factors as well as the neutral axial form factor. At the substantial momentum transfer of these measurements, theory offers little guidance about these form factors or their interrelationships. Therefore, it is essential to provide the measurements proposed here by G0 to complement the existing and anticipated (forward angle G0) data and to enable a clear and unambiguous interpretation in terms of nucleon form factors.

3 Experiment

3.1 Introduction and Kinematics

In this experiment we propose to make measurements of the backward angle parity-violating asymmetries using both hydrogen and deuterium targets. The kinematics are chosen to approximately match the range of the forward angle running while avoiding the very lowest momentum transfers (and beam energies) where the SAMPLE experiment has already made measurements [42, 46, 47]. As shown in these measurements and discussed above (Section 2), measurements involving quasi-elastic scattering from deuterium are necessary to separate the vector and axial vector currents of the nucleon. Although we are proposing measurement of a range of momentum transfers, with this submission we are requesting beam time for only a single measurement (including running on both the hydrogen and deuterium targets) at $Q^2 = 0.8$ GeV^2.

We propose backward angle measurements at three values of Q^2 (elastic in the case of the hydrogen target, quasi-elastic in the case of deuterium) to give a reasonable amount of information on the Q^2 variation of the three form factors G_E^s, G_M^s and $G_A^e(T = 1)$. The nominal central angle for the G0 spectrometer for these measurements is 110°, thus fixing the incident energies. The kinematics, (quasi-) elastic rates (for the entire spectrometer acceptance), and nominal asymmetries for these three running conditions are shown in Table 3.1

Target	E (GeV)	θ (°)	Q^2 (GeV^2)	Rate (MHz)	Asymmetry (ppm)
^{1}H	0.424	110	0.3	1.017	−18
^{2}H	0.424	110	0.3	1.391	−25
^{1}H	0.585	110	0.5	0.359	−32
^{2}H	0.585	110	0.5	0.505	−43
^{1}H	0.799	110	0.8	0.095	−54
^{2}H	0.799	110	0.8	0.137	−72

Table 3.1: Elastic and quasi-elastic kinematics, rates, and nominal asymmetries.

The new experimental aspects of this measurement (as compared to the forward angle measurements where the asymmetries are somewhat smaller) are associated with the quasi-elastic scattering from deuterium. Accordingly, in the remainder of this section, we address only the corrections necessary to extract single nucleon information from the quasi-elastic scattering as well as the requirements for particle identification accruing from the quasi-free π^- production from the neutrons in the target.

3.2 Deuterium corrections

Because the third asymmetry measurement that allows separation of the three weak form factors involves a nuclear target, there are potentially nuclear corrections to be considered. These corrections fall into two categories: contributions from processes other than quasielastic scattering, such as elastic, threshold breakup and Δ production, and those that arise in quasielastic scattering but from non-nucleonic currents in the deuteron, such as meson exchange.

The experimentally measured asymmetry can be written as

$$A_D = \frac{\sigma_{QE}A_{QE} + \sigma_{el}A_{el} + \sigma_{ted}A_{ted} + \sigma_\Delta A_\Delta}{\sigma_{QE} + \sigma_{el} + \sigma_{ted} + \sigma_\Delta} \tag{3.1}$$

where the four terms are contributions from quasielastic scattering, elastic e-d scattering, threshold breakup, and Δ production, respectively. Nucleon resonances higher than the Δ are not considered.

The asymmetry due to elastic e-d scattering was calculated by Pollock [61] and in [5], and, neglecting the small D-state contribution to the deuteron wave function, can be summarized by the expression

$$A_{el} = \frac{G_F Q^2}{4\pi\alpha\sqrt{2}}\left[4\sin^2\theta_W + \frac{2G_M^s}{(G_M^p + G_M^n)}F_T\right], \tag{3.2}$$

where $F_T = v_T B(Q^2)/(A(Q^2) + B(Q^2)\tan^2(\theta/2))$, where $A(Q^2)$ and $B(Q^2)$ are the elastic deuteron form factors, and v_T is the usual kinematic factor. The asymmetry for threshold breakup was also calculated in [5] and may be written as

$$A_{ted} = -\frac{G_F Q^2}{4\pi\alpha\sqrt{2}}\left[(2 - 4\sin^2\theta_W) - \frac{v_{T'}}{v_T}(4 - \sin^2\theta_W)\frac{M_N}{q}\frac{G_A^e(T=1)}{2G_M^{T=1}}\right] \tag{3.3}$$

where $v_{T\prime}$ is the standard kinematic factor. Although in each case there is some dependence on the unknown form factors G_M^s and G_A^e, both asymmetries are comparable in magnitude to A_{QE}. The effect of such events on A_D is negligible: in the worst case the elastic (threshold) cross sections are 3% (0.1%) of the integrated quasielastic cross sections.

The inelastic scattering contribution, which will arise primarily from Δ excitation, can potentially modify the measured asymmetry from that expected from quasielastic scattering alone and can likely not be neglected. The asymmetry in hydrogen is the subject of the proposal of S. Wells *et al.*, [62], where the formalism for parity violation in the N-Δ transition is documented. Following the notation of Mukhopadhyay, *et al.* [63],

$$A_\Delta = -\frac{G_F Q^2}{4\pi\alpha\sqrt{2}}\left[\Delta_{(1)}^\pi + \Delta_{(2)}^\pi + \Delta_{(3)}^\pi\right] \tag{3.4}$$

The two terms $\Delta_{(2)}^\pi$ and $\Delta_{(3)}^\pi$ combined are expected to be $\sim 0.2\Delta_{(1)}^\pi$, and are thus neglected for the purposes of the background calculation. The quantity $\Delta_{(1)}^\pi = 2(1 - 2\sin^2\theta_W) = 1.075$ [10]. In [64], A_Δ in a nucleus was considered. At backward angles, the dominant contribution is from quasifree Δ production, so $A_p \sim A_n \sim A_d$.

The contribution to the asymmetry from quasifree Δ production was estimated by simulating the detector acceptance for both elastically and inelastically scattered electrons in the CED and FPD arrays. These events result in two bands in FPD/CED space with very little overlap at the two lowest kinematics, somewhat more overlap at $Q^2 = 0.8$ (GeV/c)^2. The FPD/CED pairs corresponding to elastic scattering were then selected and each rate summed over all such pairs. The contribution from inelastic scattering is small except at the highest momentum transfer, where such events are expected to result in a reduction of the measured asymmetry in the elastic region of FPD-CED space of about 10%. It is important to note that, just as in the case of the hydrogen data, the inelastic asymmetry in deuterium will be measured simultaneously with the quasielastic scattering asymmetry over a range of Q^2 and ν, so it will be possible to make any necessary correction with measured inelastic asymmetries rather than relying on a calculation.

The second major class of corrections to be considered are corrections to the simple "static approximation" for the deuterium asymmetry:

$$A_d = \frac{\sigma_p A_p + \sigma_n A_n}{\sigma_d} \tag{3.5}$$

In this expression the deuteron is assumed to consist of a noninteracting neutron and proton at rest. Hadjimichael, *et al.* [7] have considered the effect of final state interactions on this expression. They performed their calculation with two nucleon potentials that represent the extremes of the state-of-the-art potentials. Near our kinematics, they find that the correction to the static asymmetry expression is small ($\sim 1\%$), and the variation between the two nucleon potentials used is also small ($\sim 1\%$). Two body currents (meson exchange currents) have been considered by the authors of refs [57, 8]. Schramm and Horowitz [57] considered heavy meson exchange corrections; they find that the correction to the asymmetry is less that 1% at our momentum transfer. More recent work [8] which also incorporates pion exchange currents also finds that the corrections are small.

Finally, there is the possibility of an asymmetry generated by a nuclear parity-violating component in the deuteron wavefunction. This effect has been calculated in refs [58, 59] and shown to be small compared to our expected asymmetries. For example, Hwang, *et al.* [59] used the DDH [60] parameters to characterize the parity-violating nucleon-nucleon interaction, and they find that the asymmetry is $A \sim 4 \times 10^{-7}$ at backward angles at 0.500 GeV for relative energy $E_{np} = 9$ MeV. The asymmetry falls with increasing E_{np}, so it will be even less significant at the quasielastic peak.

3.3 Particle identification requirements

Negatively charged pions have been found to produce a significant background to the elastic and quasielastic rates detected by the G^0 spectrometer at backward angles. The pions are produced mainly by photoproduction near the Δ-resonance. In the case of a hydrogen target, single π^- photoproduction is forbidden by kinematics; two pions must be produced in order to see a single π^- in the spectrometer. However, in the case of a deuterium target, single π^- photoproduction occurs due to the presence of neutrons.

This background is found to dominate over quasi-elastic rates from deuterium at backward angles. The background can be kinematically separated from elastics in the hydrogen target case, but tends to overlap with the inelastic electrons in the measurement of the parity violating asymmetry in the $N \rightarrow \Delta$ transition [62]. It is therefore desirable to have an additional particle identification detector for the backward angle experiment.

3.3.1 Calculation of π^- Cross Sections

The process of π^- photoproduction from the neutron can be simulated using photoproduction cross-sections with the appropriate Bremsstrahlung and virtual photon fluxes. These processes were used both for the deuterium itself and for (quasi-free) production from the aluminum target windows in each case.

For the virtual photon contribution to the cross section, the MAID [65] parameterization of the transverse photoproduction pion cross section was used with a virtual photon flux [66] and appropriate Jacobian factors. Fermi motion was included in the model, using Monte Carlo generation of initial state nucleon momenta, according to a nucleon momentum distribution obtained from a fit of inclusive quasi-elastic scattering data.

For the Bremsstrahlung photon contribution to the cross section, the GRAAL Monte Carlo generator was used [67]. This generator was found to be in good agreement with a model using the photoproduction cross section from MAID and the Bremsstrahlung photon spectrum of Ref. [68]. The GRAAL Monte Carlo code has the additional capability of simulating two-pion production.

These cross sections were also tested against the commonly used code of Lightbody and O'Connell (LBOC) [69]. For kinematics similar to those encountered in G^0, the MAID and GRAAL results were found to be a factor of 3 to 4 larger than those given by the LBOC code. This was determined to be due to the older pion photoproduction cross-section parameterization used in the LBOC code, and due to bugs in the LBOC code.

3.3.2 Measurement of π^- Rate at Backward Angles

To test the pion photoproduction cross-section calculation in kinematics similar to those planned for G^0 backward-angle running, a facility development request to use the Short-Orbit Spectrometer (SOS) in Hall C was generated. During a parasitic run on October 27-29, 2000, π^- photoproduction cross sections from hydrogen, deuterium, and carbon targets were measured. Elastic and quasielastic cross-sections were also measured. For these measurements, the beam energy was 0.824 GeV, and the SOS angle was fixed at 136.5°. Rates for negatively charged particles were measured in the momentum range 150 to 400 MeV/c. The beam current averaged 20 μA. Data for hydrogen and deuterium were taken with two different target lengths (4 and 15 cm) to test the ability of the calculations to accurately predict the fractions of the total pion rate due to virtual photons and Bremsstrahlung photons.

The results and analysis of the pion data from this run are reported in a G^0 internal note [70] and will be summarized here. The measured π^- cross sections from hydrogen are

shown in Fig. 3.1. The cross section is compared with a calculation using the GRAAL

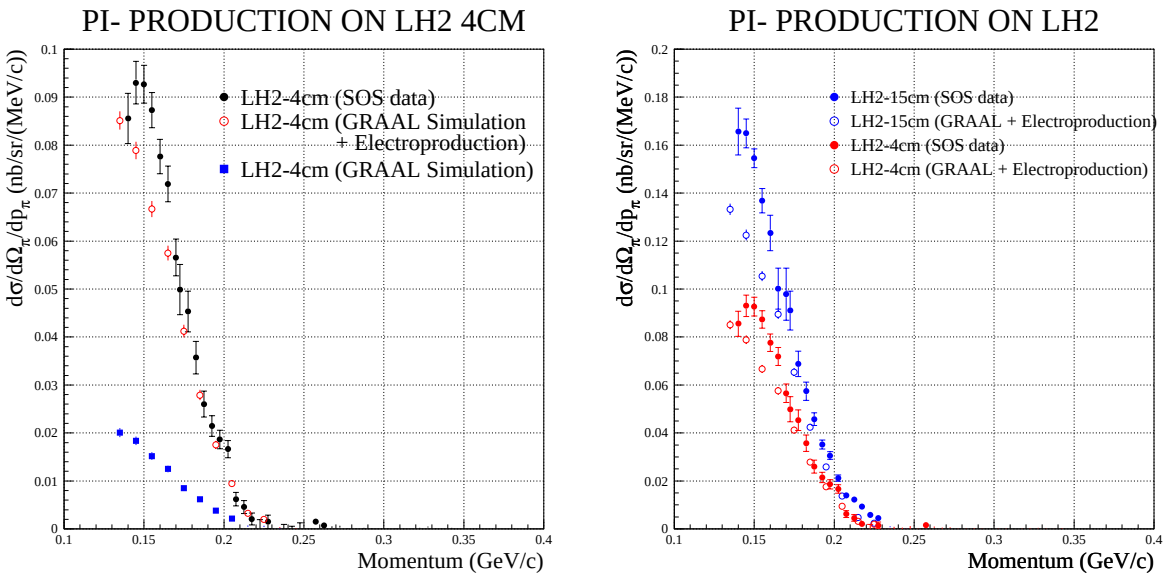

(a) (b)

Figure 3.1: Comparison of data and simulation of π^- production from (a) 4 cm and (b) 15 cm LH_2 targets.

code. The breakdown of electroproduction and photoproduction pieces of the cross section in the simulation is also shown. The disagreement at lower momentum is believed to be due to the fact that the GRAAL code does not presently simulate virtual photons below a certain Q^2. The G^0 spectrometer will generally select pions of higher momentum, so the agreement is sufficient to be able to use the code to generate two pion production for simulation of backgrounds in the experiment.

The measured π^- cross sections from deuterium are shown in Fig. 3.2. The cross sections are compared with the simulation using the GRAAL code for pion photoproduction and the MAID-based calculation for pion electroproduction. The cross section is dominated by single π^- production. The agreement of the data with the calculation is excellent, indicating that the cross section for the G^0 case is well understood.

The ratio of the pion rates from the 15 cm and 4 cm liquid hydrogen and liquid deuterium was found to be roughly 1.6, in agreement with arguments based on the radiation length of the target and the equivalent radiator for virtual photons at these kinematics.

3.3.3 Pion Rates and Contaminations

Pion rates for G^0 backward angle running were determined using the models of the cross section tested in the previous section, along with a GEANT-based model of the G^0 acceptance [71].

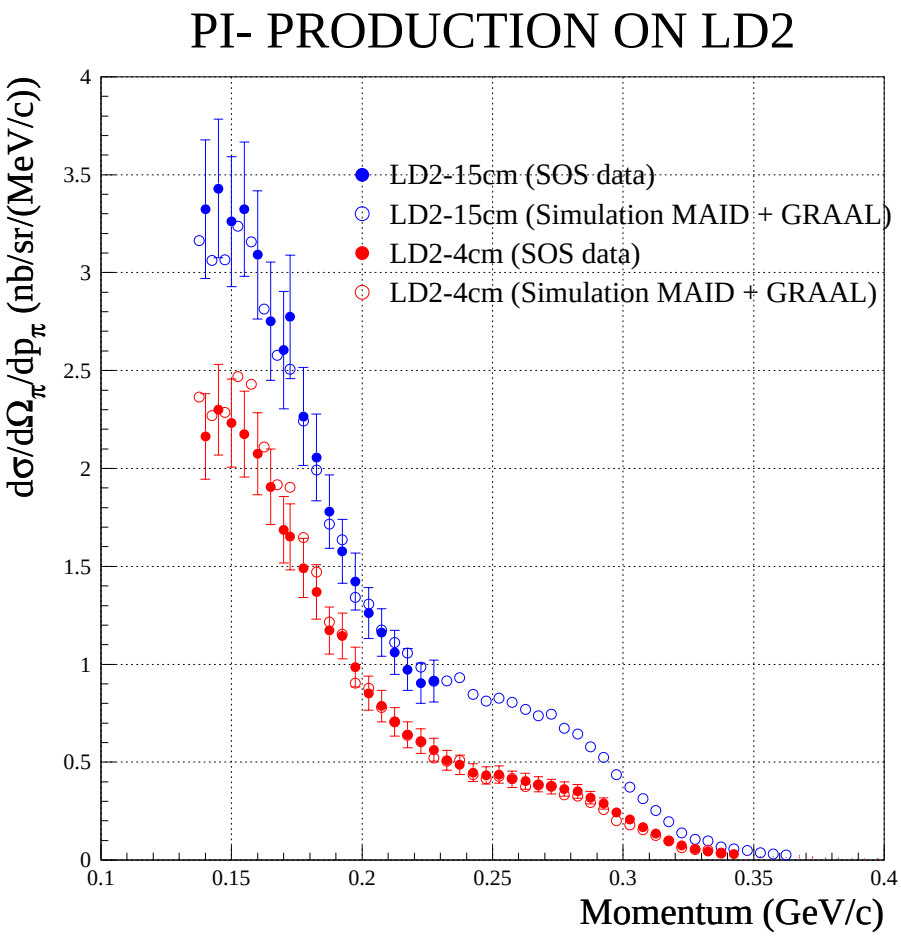

Figure 3.2: Comparison of data and simulation of π^- production from 4 cm and 15 cm LD_2 targets.

The pion rates for the liquid hydrogen target running are found to be largest relative to the elastic rate for the proposed beam energy of 0.799 GeV. The pion, elastic electron, and inelastic electron rates for 0.799 GeV are shown in Fig. 3.3. Rates are proportional to the size of the box shown for each CED and FPD combination. The rates assume a 20 cm long target and 40 μA beam current. Tracking of all secondaries was included. Muons resulting from pion decay are also included in the pion rates. At 0.799 GeV, muons present 15% of the total flux of pions and muons at the location of the CED. At 0.424 GeV, 20% of the total flux is due to muons. The pion rates are found to be roughly 25% of the elastic rate along the locus of the elastic curve at 0.799 GeV.

The pion rates for LH_2 running are dominated by contributions from the aluminum target windows. For this simulation, only the contribution of virtual photons interacting with the target windows was included, and final state effects and Fermi motion were ignored. Inclusion of real photons increases the pion rate by a factor of 1.5, but final state interac-

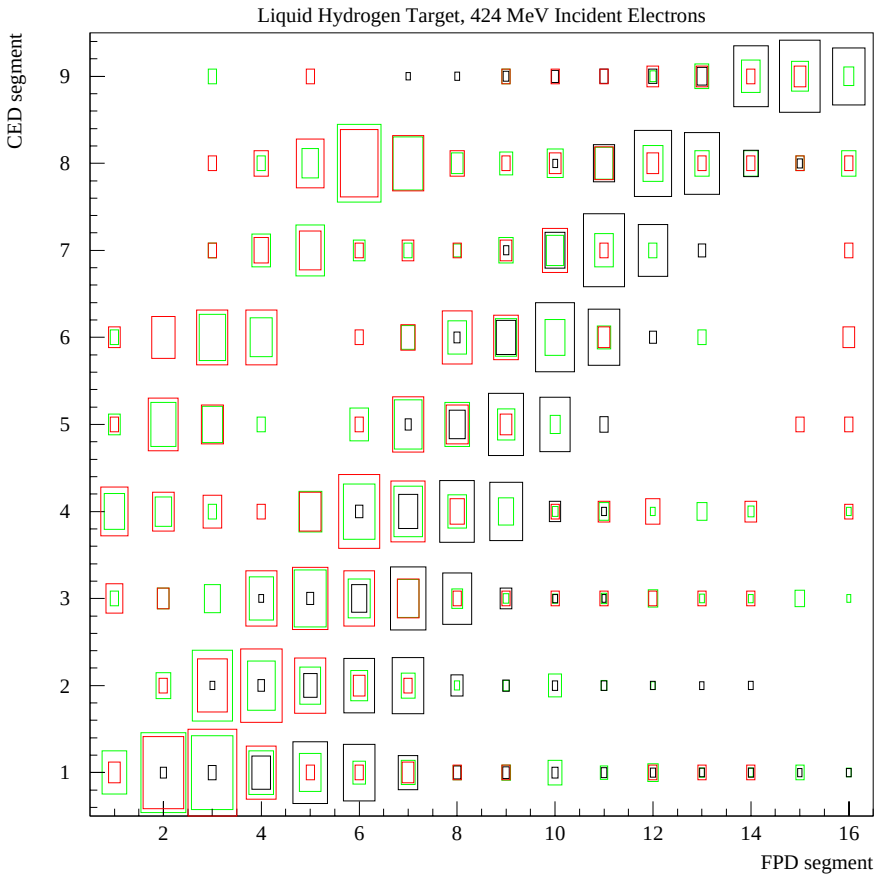

Figure 3.3: Relative CED and FPD rates for one octant of the G^0 spectrometer, LH_2 target, for beam energy 0.799 GeV. The coincidence rate is proportional to the size of the box. Elastic e^- rates are shown in black, inelastic e^- rates are shown in red and estimated π^- rates are shown in green.

tions should reduce the cross section by roughly 50%, so these two effects roughly cancel. The effect of Fermi smearing does not change the overall rate, but causes the pions to have more overlap kinematically with the elastic electrons. The effect of this will be discussed later.

The π^- rates for LD_2 running are shown in Figs. 3.4(a), (b), and (c) for the proposed beam energies of 0.424, 0.585, and 0.799 GeV, respectively. As expected, the negative pion rates are considerably larger for liquid deuterium. The aluminum target windows account for roughly 1% of the total rate, with the remaining 99% being roughly equally divided between contributions from virtual photon and Bremsstrahlung photon fluxes to the π^- photoproduction cross section from the LD_2 in the target itself. There is a large

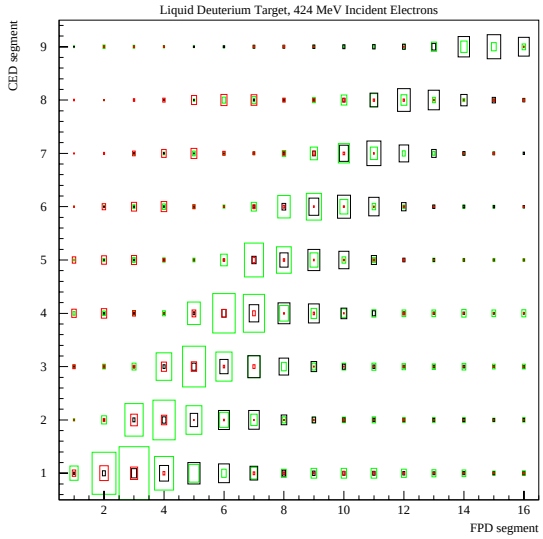

(a)

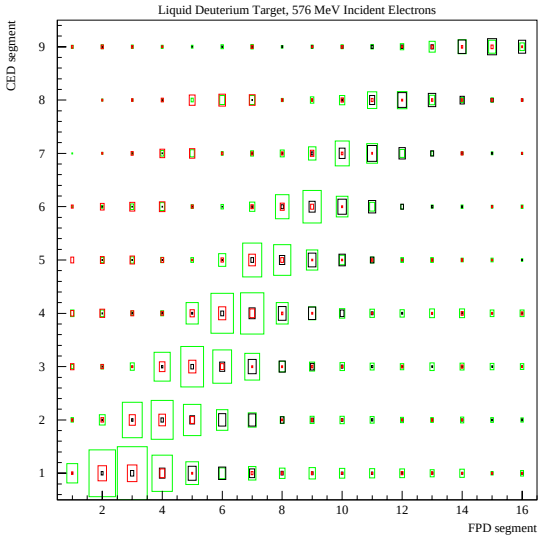

(b)

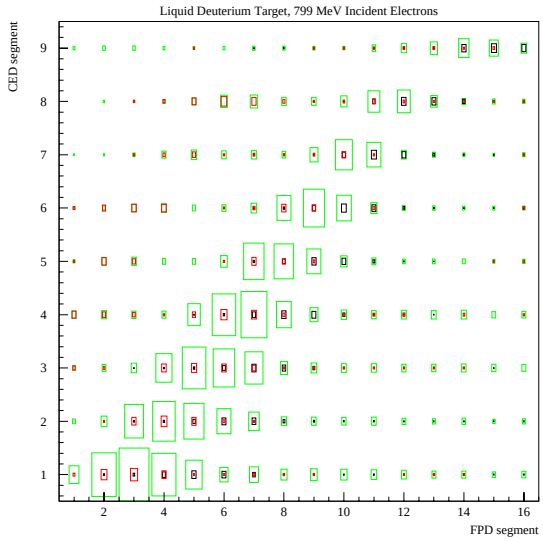

(c)

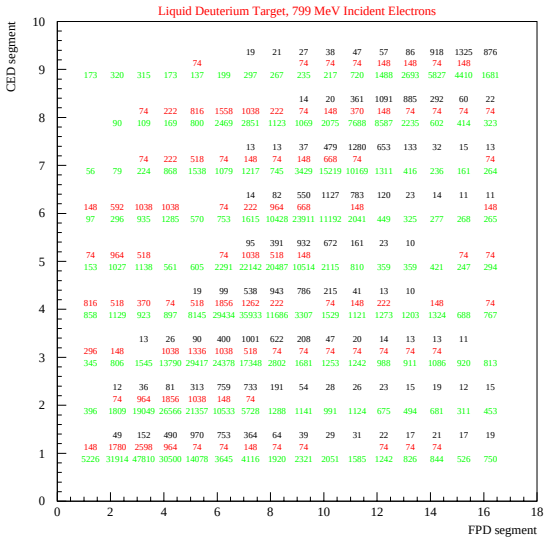

(d)

Figure 3.4: Relative CED and FPD coincidence rates for one octant of the G^0 spectrometer, LD_2 target. The coincidence rate is proportional to the size of the box. Quasi-elastic e^- rates are shown in black, inelastic e^- rates are shown in red and estimated π^- rates are shown in green. (a) 0.424 GeV, (b) 0.585 GeV, (c) 0.799 GeV. Figure (d) contains the rates for 0.799 GeV, in text form.

pion contamination in all three cases, preventing the measurement of the quasi-elastic asymmetry for the deuteron.

Selecting certain CED and FPD combinations allows the optimization of the elastic/inelastic separation. The same selection procedure also helps to exclude pions from the elastic sample. Table 3.2 summarizes the pion contaminations expected for the proposed kinematics, satisfying the same cuts used to separate elastic from inelastic electrons described in Section 2. As mentioned earlier, the pion contamination for the liquid hydrogen

E_{beam}	$(\pi+\mu)/e$ ratio	
(GeV)	LH_2	LD_2
0.424	0.013	0.39
0.585	0.042	1.6
0.799	0.25	8.4

Table 3.2: $(\pi+\mu)/e$ ratio expected for same CED and FPD combinations used in Section 2 to attempt to separate elastic from inelastic electrons. Here only elastic and quasi-elastic electrons are counted in the denominator.

target running is dominated by contributions from the target windows. The contribution from two-pion production in the liquid hydrogen target itself to the total pion rate is 15% at 0.799 GeV, but is negligible at lower energy. As mentioned earlier, the effect of Fermi-smearing of the kinematics of these pions was neglected. Fermi smearing of the pion kinematics has been estimated to give roughly a factor of 2 increase in the contamination, for the lowest beam energy proposed. The relative size of the effect will be smaller at higher energy, as the Fermi momentum becomes small relative to the beam energy. The estimated pion contaminations for LH_2 should therefore be accurate to the 50% level.

The pion contamination for LD_2 was calculated including Fermi motion. The contamination is found to be too large to make a measurement of the quasi-elastic asymmetry in deuterium. The pion to elastic electron ratio is 8.4:1 in the worst case. A measurement of the quasi-elastic asymmetry is therefore impossible without additional particle identification. A particle identification detector must provide a pion rejection of better than 100:1, to reduce the worst-case pion contamination to the level of 10%.

The pion contamination of the inelastic electron rate from LH_2 is obviously worse than for the elastic case. The proposed measurement of the parity violating asymmetry in the $N \rightarrow \Delta$ transition [62], using the LH_2 running, would therefore also benefit from additional particle identification [72].

3.3.4 Rejection of π^- Background

The kinematics of the pions and muons which need to be rejected for each proposed beam energy are shown in Table 3.3.

The type of detector affording the best π/e discrimination at these energies and being implemented with the most ease in the current G^0 geometry is an aerogel Čerenkov counter.

E_{beam} (GeV)	p_π range (MeV/c)	$\beta_\pi^{\max}$	p_μ range (MeV/c)	$\beta_\mu^{\max}$
0.424	100 - 250	0.87	50 - 225	0.90
0.585	100 - 300	0.91	50 - 275	0.93
0.799	100 - 375	0.94	50 - 350	0.96

Table 3.3: Pion and muon kinematics for each spectrometer setting. Recall that muons account for less than 20% of the total pion and muon flux.

The index of the aerogel should be less than $1/\beta$ from above, but should be as large as possible to maximize light yield. It is therefore found that $n = 1.03$ is a good choice.

An aerogel Čerenkov counter should also be able to give the requisite better than 100:1 pion rejection.

The design and prototyping of a Čerenkov counter for G^0 will be discussed in Section 4.1.3.

4 Apparatus

4.1 Detectors

The detector system to be used for these backward angle measurements consists of two arrays of scintillators and an aerogel Cerenkov detector for each of the eight G0 octants. The two scintillator arrays comprise: a Focal Plane Detector (FPD) array (sixteen detectors per octant each viewed from two ends), which will also be used for the forward angle measurements, and a Cryostat Exit Detector (CED) array (nine detectors per octant each viewed from two ends). For backward angle electron detection, both arrays are required to determine the electron scattering angle and momentum, thereby providing an adequate separation between elastically and inelastically scattered electrons. The Cerenkov detector is required to reduce the contribution of π^-'s, particularly important during running with the deuterium target.

4.1.1 FPD's

In the forward angle measurement, back-to-back pairs of FPD scintillators are used to detect protons. In the back angle measurement 16 single FPD scintillators will be paired with CED scintillators to detect elastic and inelastic electrons as indicated below (the back element of each FPD pair will not be used in the back angle measurement). A photograph of completed North American (NA) and French FPD octants is shown in Figure 4.1; the octants supported from a detector support ("ferris wheel") shown in Figure 4.2. Each FPD scintillator has a curved shape roughly 60 - 120 cm in length and a width of 5 - 10 cm. The first four FPD elements are 5 mm thick; the remainder have a thickness of 1 cm. Each is connected to a pair of photomultiplier tubes via lucite lightguides. The measured yield at each phototube is of order > 75 p.e. for minimum ionizing particles.

4.1.2 CED's

The CED's are a critical component of the G0 backward angle running, and here we provide a summary of the progress to date on this detector package. In the original proposal, there were to be twelve individual CED's per octant, to be combined with the sixteen FPD's. Due to space constraints between the magnet end cap, beam line shielding, and the FPD octant support, three of the CED's closest to the beam line were eliminated from the design, leaving nine CED's per octant. Because the three CED's which were removed intercepted a large yield of lower momentum inelastically scattered electrons, our momentum transfer range for the $N - \Delta$ measurement does not reach as low as originally proposed, and our statistical uncertainty at lower momentum transfer is somewhat larger than originally expected.

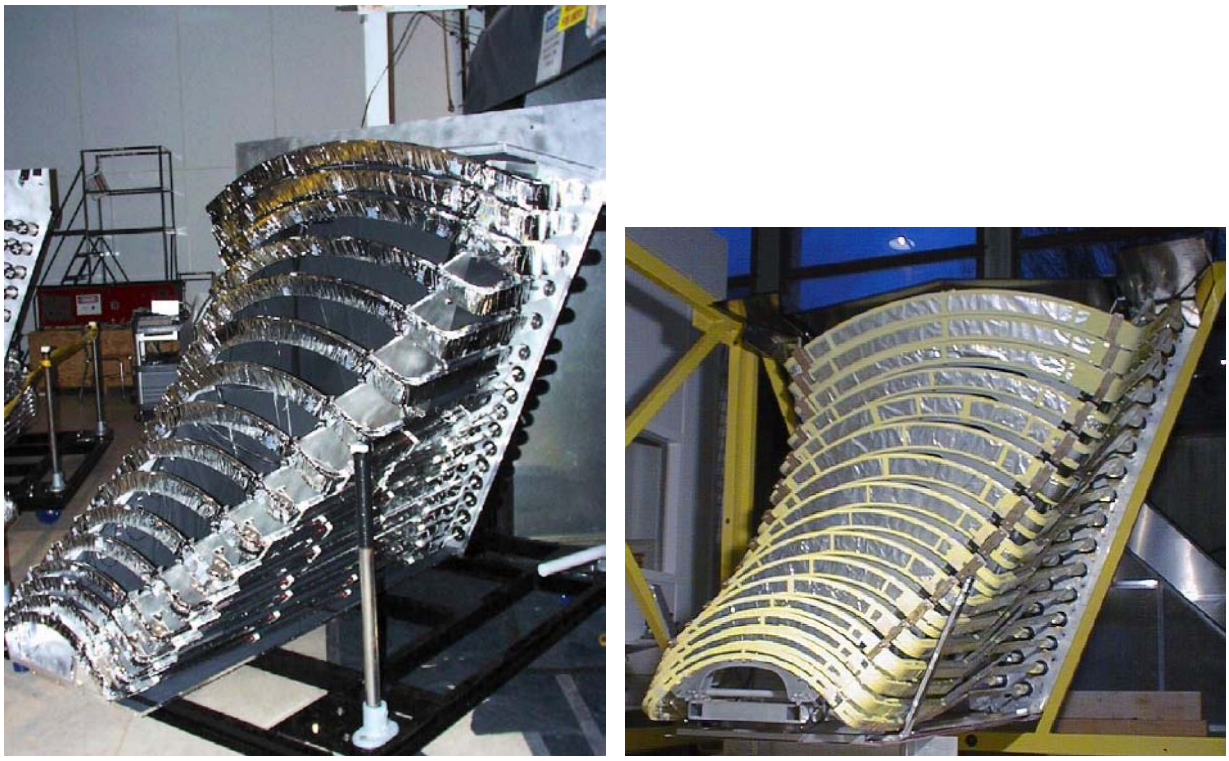

(a) (b)

Figure 4.1: Photograph of complete sets of FPD's mounted into the FPD octant support; a) North American b) French.

The design of the remaining nine CED's has been completed, including the shapes of both the scintillators and light guides, and a procedure for manufacturing the correct shapes for the light guides has been developed and tested in the construction of a prototype CED. A detailed simulation of expected light yield from these detectors was performed, and the number of photoelectrons predicted was found to be more than adequate for these measurements. A prototype CED was constructed at TRIUMF, and tested at Louisiana Tech University using the same PMT/base assemblies to be used in the North American FPD's, and the amount of light collected was consistent with the predicted amount, i.e. more than adequate for these measurements [73, 74].

The construction of the CED's has just begun in the TRUIMF scintillator shop. All of the scintillator material has been purchased and shipped to TRIUMF, and approximately one half of the light guide material is presently on hand. As demonstrated in the construction of the prototype CED, the procedure to obtain the correct shapes for the scintillators is well determined. The current schedule calls for delivering the cut and polished scintillators and light guides to JLab in the December of 2001, when assembly of the detectors will begin.

Figure 4.2: Photograph of "ferris wheel", with one octant support installed, along with one collaborator to set the size scale.

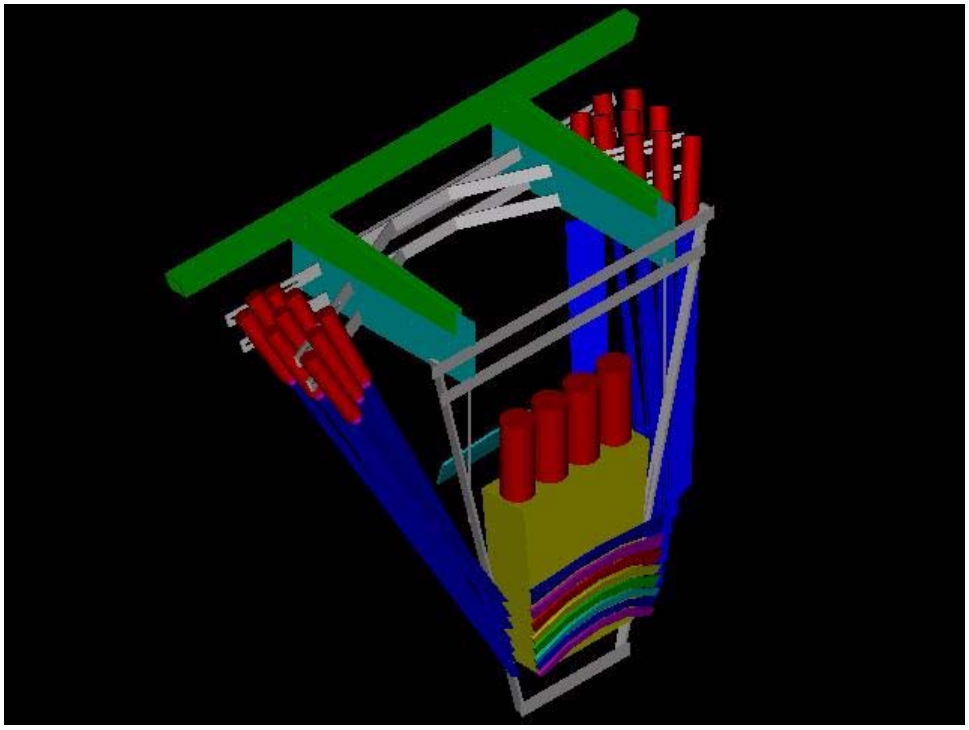

Figure 4.3: Schematic diagram of the CED octant support structure, showing the relative locations of the scintillators, light guides, and PMT's. Also shown is the relative position of a Čerenkov detector for backward-angle measurements.

The design of the octant support structure for the CED's is presently underway. The conceptual design, a schematic of which is shown in Fig. 3, is complete, and takes into account both the required mechanical support of the CED scintillator/light guide/PMT and base assemblies, as well as the relatively weak alignment constraints on these detectors. Also shown in this figure is the relative positions and shapes of the CED's, light guides, and PMT's. Each octant support will be attached to the outer ring of the "ferris wheel" to provide the main mechanical support, in the region of the CED assembly near the PMT's where the majority of the weight of these detectors resides. The positioning of the scintillators, as well as additional mechanical support, is obtained through the use of cantilevered struts extending from the main support through the region near the bend in the light guides outside of the acceptance of the scattered electrons. This octant support design will be integrated with the support structure for the Čerenkov detectors, the design of which is also presently underway. We discuss the Čerenkov detector and its support structure in the next section.

4.1.3 Aerogel Cerenkov

The π^- background from $(n(e,\pi^-)e'p)$ will be reduced by introducing cuts in CED-FPD space, but not to a level sufficient to isolate quasi-elastic electrons. Therefore an aerogel Čerenkov detector has been designed to provide excellent pion rejection across the full G0 momentum range, up to $\sim$ 400 MeV/c for $Q^2 = 0.8$ GeV^2. This, of necessity, must

be an eight-sectored array of individual Čerenkov detectors mounted in conjunction with the CED-FPD sectors. This implies the construction of an 'extension' to the detector supporting 'ferris wheel'. The geometry of the aerogel Čerenkov detector is shown in Figure 4.4.

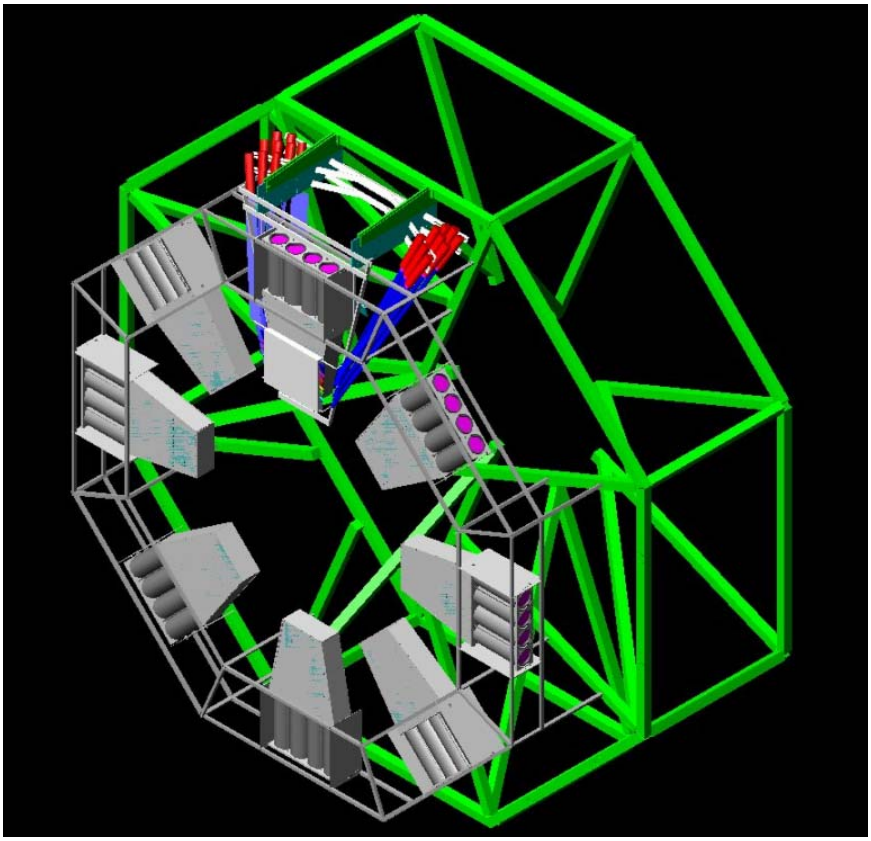

Figure 4.4: Concept of the full eight-sectored G0 backward angle set-up. The top sector shows the full detector arrangement: CED, Čerenkov and FPD. The others show the Čerenkov detectors only along with the 'ferris wheel' support frame.

A single octant detector is shown in more detail in Figure 4.5.

Negatively charged particles entering an octant of the G0 spectrometer pass through 5 cm of aerogel. The aerogel has a proposed index of refraction $n = 1.03$, so that a particle with a speed such that $\beta > \frac{1}{1.03}$ will produce Čerenkov light. Thus, pions up to a momentum of 570 MeV/c will not produce any light. On the other hand, all primary electrons will produce light. Thus the detector will operate in *coincidence* mode and not in *veto* mode.

The light is emitted within a small angle ($cos\theta_c = \frac{1}{1.03}$ at max.) and enters a downstream region whose walls are lined with a white diffuse reflector. The likelihood of a photon reaching one of four phototubes is related to their active area compared to the total internal area of the light box, which is a little better than 4%. Other goals in the boxes design are to cover as large a fraction as possible of the G0 acceptance while keeping the timing spread as narrow as possible.

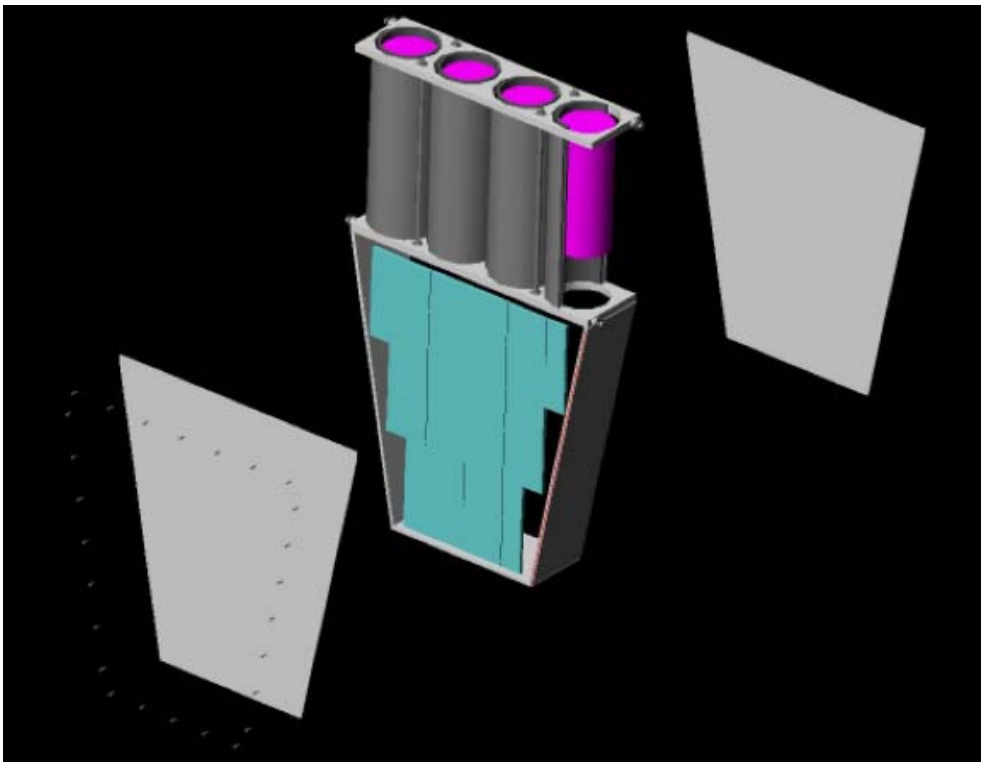

Figure 4.5: A view of the concept of a single octant light-box with aerogel Čerenkov radiator and PMT's

With 5 cm of clear aerogel, the electrons are expected to give about 6 photoelectrons; whereas a 400 MeV/c pion would have a rejection factor of $\frac{1}{125}$. This latter pion signal appears to arise mostly due to δ-rays produced in the CED's or elsewhere.

The phototubes for the Čerenkov counter for each octant will be tied together to produce one summed signal. This signal will be discriminated and ANDed into the trigger. Using existing sampling techniques, Čerenkov ADC spectra could be used to check the calibration and pion rejection factor of each octant.

The typical time-width of the signal from an aerogel Čerenkov of this design is $\sim$20 ns (due mainly to collection time in the light box), during which time the radiator is 'dead'. This is because the light can bounce around in the box for some time. The rise time of the pulse is of the order of 1 ns. Beam pulses from JLab are delivered to the experiment every 32 ns. If the event time of the detector were larger than 32 ns, the event after each trigger would have to be vetoed (which is the plan for the forward angle measurements).

Studies with both Monte Carlo simulation and a simple mock-up of the Čerenkov counter have been done. The various sub-groups are also planning the construction of a more realistic prototype. Most of the assumptions above come from tests and simulations performed by the Caltech group and Grenoble simulations [75, 76]. At Caltech, a small Čerenkov test counter using a single phototube was built for the purpose of testing light yield and timing

calculations from Monte Carlo simulations based on Ref. [77], and was found to produce results similar to the simulation. The test counter is currently being used to study various design parameters (aerogel thickness, light-box dimensions, light-box lining, etc.), using cosmic rays. Collaborators at Caltech are also constructing a full-sized prototype, to be tested using cosmic rays over the summer.

At TRIUMF designs for both the detector octant (light-box) and the support (extension to the Ferris Wheel) have been developed. The detector prototype project will be released to the TRIUMF shop very soon; cosmic ray tests should begin by the end of June. A proposal has been submitted to the TRIUMF administration (TRIUMF "Experiment" 911) to use the TRIUMF M11 beam to test the prototype. An "electron" beam of $\beta \simeq 1$ (say 50-80 MeV/c) to characterize the response of the aerogel detector as a function of angle and position. A 400 MeV/c pion beam will be used to determine the rejection efficiency for pions. This can be investigated as a function of the material in front of the detector (as δ-rays are believed to be the primary cause of false signals from the pions). Measurements can also be made at other momenta to characterize the detector response and confirm the simulations. The beam-time is likely to be in the late Fall (November or December) of 2001.

4.2 Electronics

As in the case of the forward angle measurements the four French octants will be instrumented using electronics developed at IPN-Orsay (DMCH-16X boards, based on flash-TDC and DSP technology), while the North American octants will be instrumented with the original Latching Time Digitizer (LTD) design. In both designs, much of the electronics used for forward-angle measurements will also be used for the backward-angle running. In particular, all of the PMT/base assemblies and associated power supplies used for the backing scintillator array for the FPD's will be used for the CED's, and all of the instrumentation for the backing array (e.g., analog splitters, constant fraction discriminators, mean timers, and ADC and TDC channels for the monitoring electronics) is also available for the CED array.

The philosophy of the backward-angle electronics design is based in large part on the fact that the electrons being detected ($E_{scattered} \geq 200$ MeV) are all moving with approximately the same velocity, and therefore have a well defined flight time for each CED and each FPD. This is shown in Figures 4.2 and 4.7, where we plot the flight time from the target to selected CED's and FPD's, respectively. Thus, a relatively tight time correlation can be made between a given CED and FPD pair and the arrival time of the beam at the LH_2 target. Consequently, the use of fast Programmable Logic Devices (PLD's) can provide hardware coincidences which can significantly reduce time uncorrelated backgrounds.

The North American electronics chain for forward-angle measurements is shown schematically in Figure 4.8. For the backward-angle measurements, the PMT's for the FPD backing detector array will be attached to the CED's, and the LTD's and "munger" redistribution boards will be replaced by custom logic circuitry being developed at Louisiana Tech. Thus,

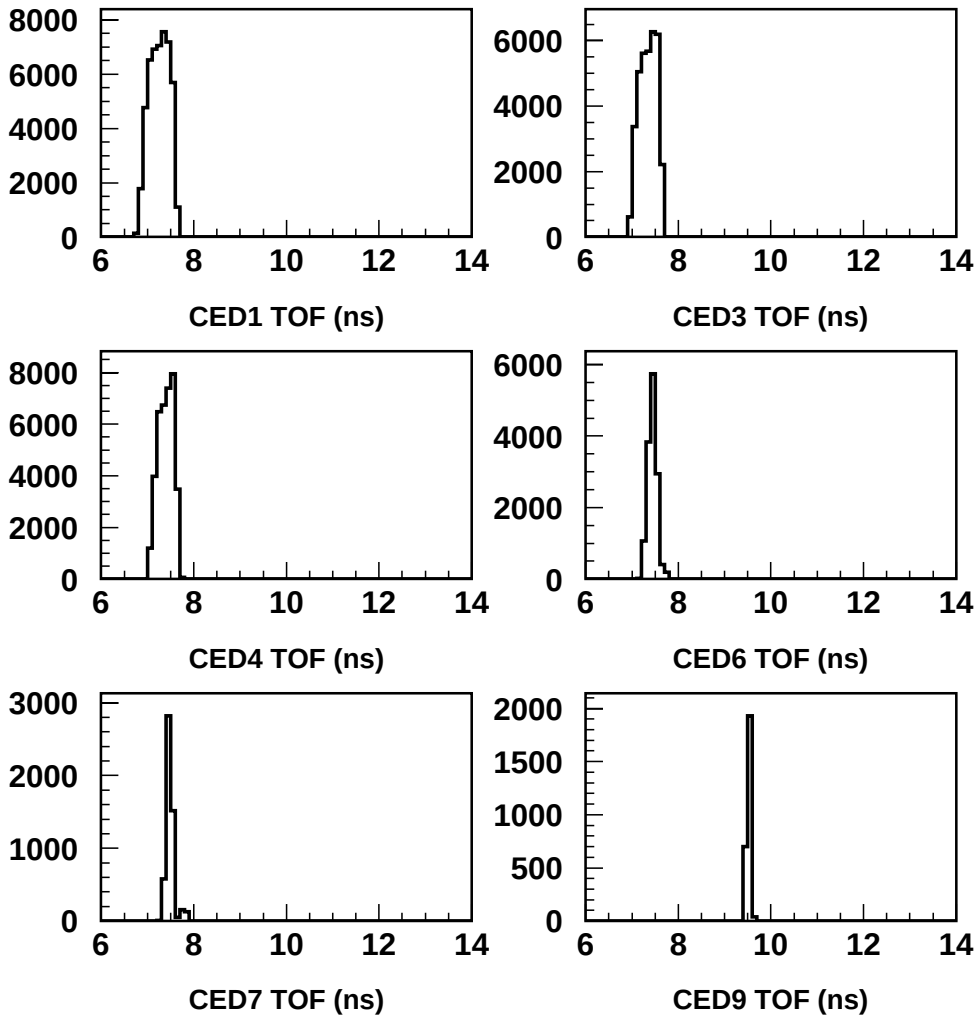

Figure 4.6: Flight times for electrons from the target to selected CED's.

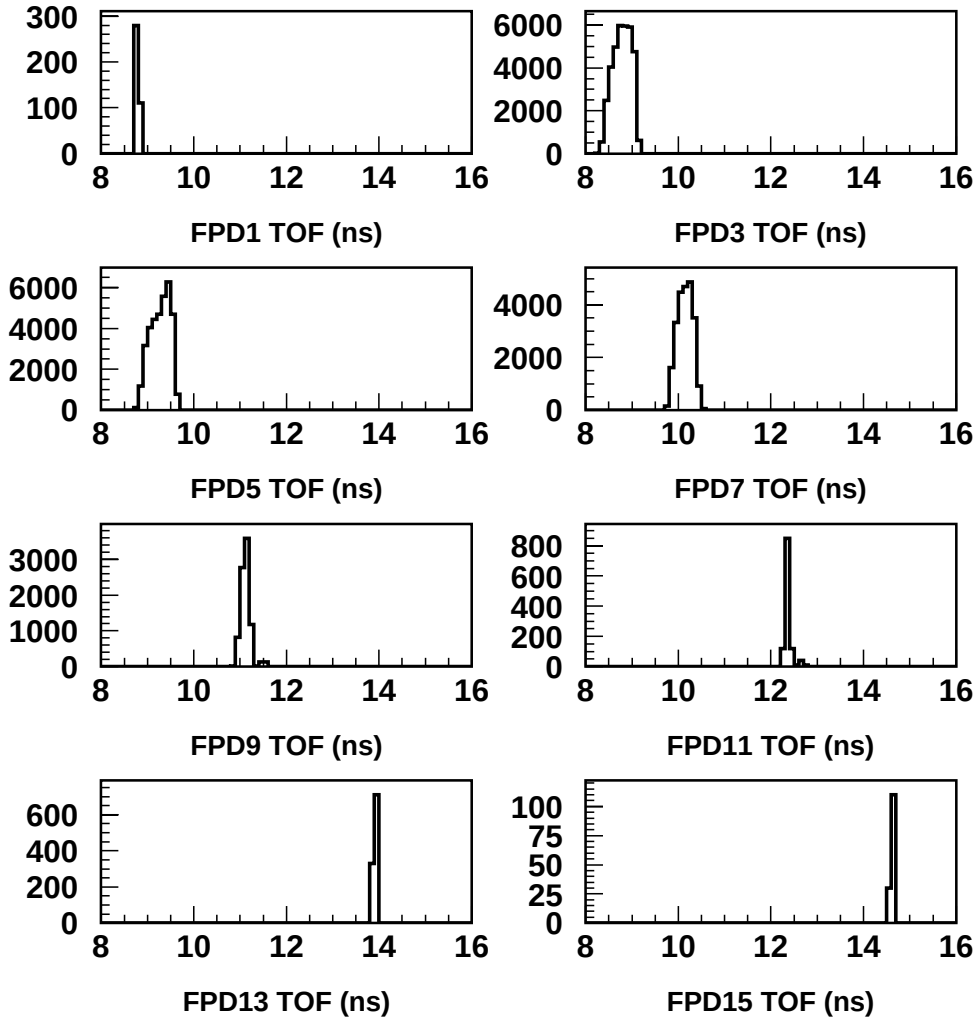

Figure 4.7: Flight times for electrons from the target to selected FPD's.

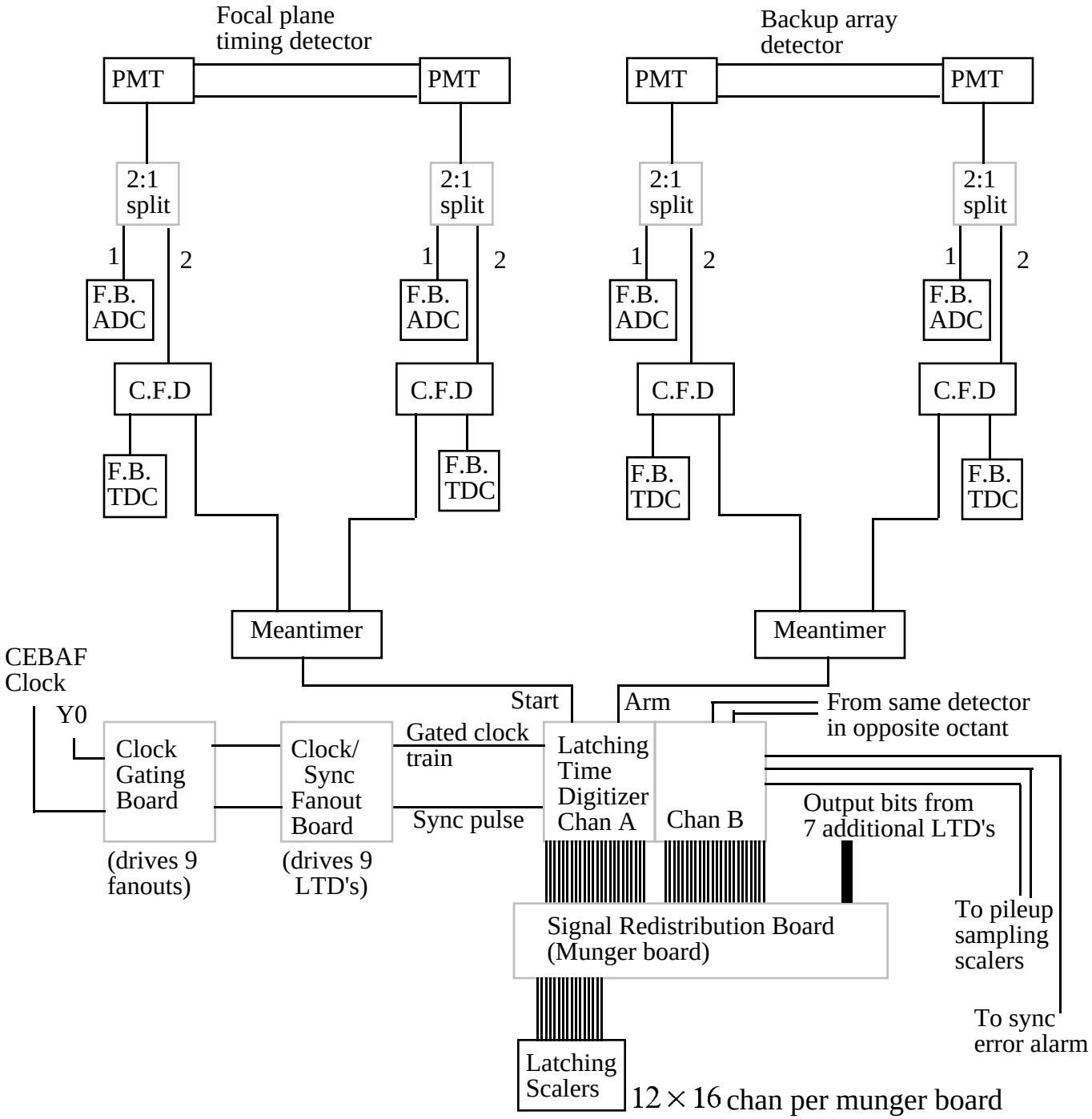

Figure 4.8: Electronics block diagram for the forward-angle running mode for the North American octants.

the input to this new logic circuitry is the output of the mean timers for both the FPD's and CED's, a discriminated signal from the Čerenkov detector, and a synchronization pulse which signals the arrival of the beam at the G0 target. The output of this new circuitry is sent to the latching scalers to count the number of coincidences between detectors in the CED array and those in the FPD array.

Significant development on the coincidence logic circuitry for the North American octants has taken place since the time of the original proposal. The circuit design, which is now complete, involves the use of PLD's mentioned above, programmed to implement all of the logic associated with the CED-FPD coincidences; the handling of "multiple hit" events (where more than one CED or more than one FPD fires on a given beam burst); and dead time monitoring. The synchronization pulse, originating from a Beam Pick Off (BPO) monitor just upstream of the G0 target, can provide a sufficiently small time window (of order 8 ns, compared with the 32 ns time between successive beam bursts arriving at the G0 target) to enable the CED-FPD coincidences at the correct time of electron arrival at these detectors. The logic signal from the Čerenkov detector, which signifies that it was in fact an electron which fired both the CED and FPD involved in the coincidence, will be used to enable a latch which allows the coincidence information to be sent to the scaler modules. Additional counting of CED and FPD singles rates, with various combinations of multiple hit logic and Čerenkov signals included, will be used for an estimate of the front end electronics dead time.

Enough of the PLD's have been obtained to construct all necessary prototype circuit boards; the programming software to burn these chips has been obtained, debugged, tested, and used for programming; and properties of the programmed PLD's as well as the logic contained in the programs have been tested. The board layout for the prototypes is complete, and these boards have been manufactured by a vendor. Stuffing and testing of these prototypes is now underway. In the final configuration, a total of five boards will be needed per octant: one to handle the coincidence logic encoding; one to handle the multiple hit, Čerenkov, and dead time information; and three to handle TTL-ECL conversion to provide the appropriate level required by the latching scalers. All of the boards will be housed in a custom VME chassis which provides the necessary power and common ground to each.

Nearly identical logic and overall philosophy will be used for the French electronics. For one octant, the front end instrumentation (discrimination and meantiming) will be handled by two DMCH-16X boards. The meantimed outputs, available on the front panel, will be sent to a CED-FPD coincidence module (designed by the Grenoble group).

The coincidence board contains all Programmable Logic Devices and scalers needed for the counting of individual coincidences between each CED and each FPD. As in the North American design, the CED-FPD coincidences will be allowed during a short time window (~ 8 ns) compared to the 32 ns beam pulse period, and the Čerenkov counter will provide an enable signal for the counting. Also as in the North American design, additional counting associated with the singles rates in the CED's and FPD's will be used for the estimate of the number of multiple hit events and for deadtime monitoring. In addition to the singles counting available in the coincidence board, the DMCH-16X modules also provide the time of flight information for the individual CED's and FPD's, which can be used for an accurate estimate of the number of lost events due to the deadtime of the front end electronics.

One CED-FPD coincidence module will be able to handle two octants. For the four french octants, the VXI crate will therefore support eight DMCH-16X and two CED-FPD coinci-

dence modules. The final design of the CED-FPD coincidence module is in progress, and one prototype will be available in November 2001.

4.3 DAQ

The data acquisition requirements for the backward-angle running configuration are almost identical to those for forward-angle running. Only small differences in the data stream will be present for both the North American and French octants.

Generally, the data stream will consist of two different types of events: high statistics data counting all particles detected within each $\frac{1}{30}$ s macropulse period and read out at 30 Hz after being latched during a ~ 200 μs interval during which time the helicity Pockels cell may change polarity; and low statistics monitoring data including ADC and TDC spectra for each PMT on each detector read out at ~ 1 kHz.This is true for both forward and backward running configurations. There will in fact be less data arising from the monitoring electronics in the backward-angle running than in the forward-angle mode, simply because there are only 9 CED's instrumented per octant (corresponding to 18 ADC and TDC spectra per octant) in contrast to 16 FPD backing detectors instrumented per octant in the forward-angle configuration. The small differences arising between the two running modes occur in the high statistics data only for the French octants, with no difference in the data streams for these events for the North American octants between the forward and backward running modes. To understand these differences, we review the data obtained for both types of instrumentation, and for both running configurations.

In the North American octants, the LTD boards discussed in the previous section are designed to separate the data obtained from each FPD for the forward-angle running into time bins within the 32 ns period between successive beam bursts. High speed scalers will then be used to store the time spectra. For the backward-angle running, no time encoding is necessary because all backward scattered electrons are moving with approximately the same speed, and it is impossible to separate elastically scattered electrons based on time of flight information. Thus, of the available scaler channels that were used for time bin counting during the forward-angle running, some will be used to count the number of coincidences between each CED and each FPD, and the remaining scaler channels will be used to count singles rates in each CED and FPD, with various constraints of multiple hits and Čerenkov detector firing. Different CED-FPD combinations correspond to different electron momentum, which allows an identification of the elastically and inelastically scattered electrons independently.

In the French octants, the high statistics data for the forward-angle measurements are sorted into time of flight histograms directly on the DMCH-16X boards through the use of flash TDC's and DSP's. These histograms are then sent into the data stream during the data read out every $\frac{1}{30}$ s through the VXI crate backplane. For the backward-angle measurement, the main information will come from scalers containing the CED-FPD coincidences and CED and FPD singles rates with multiple hit and Cerenkov constraints. The number of scalers needed is about the same as in the North American scheme.

For the estimate of losses due to the deadtime of the front end electronics, the time histograms associated to the CED's and FPD's will also be recorded. The time resolution and then the number of channels used can be adjusted compared to the forward angle measurement (from 128 to 64 or 32) in order to reduce the size of the data stream associated to the time information. Thus, the size and structure of the high statistics data events for the French octants will be somewhat different for the backward-angle measurements than for the forward-angle running.

Although there will be very little change in the data acquisition software for the backward angle running, there will be some change required to the analysis software. In the forward mode, the primary analysis involves construction of time-of-flight histograms from the North American scaler electronics or from the Orsay TDC data. Asymmetries are calculated for each detector from identification of the proton timing peak in the TOF spectrum. Since in the backward mode, in both the North American and French octants, the primary means of identifying events will now be scalers counting yields in each FPD/CED pair, asymmetries for each FPD/CED pair will be calculated from the scaler values. The processed data will thus be a two dimensional array of asymmetry values in FPD/CED space. Elastic and inelastic regions in FPD/CED space will be identified from the scaler yields.

4.4 Target

The backward angle running of the G0 experiment will utilize a slightly modified configuration of the liquid hydrogen target that has been constructed for the forward angle measurements. The baseline requirements for the G0 target are (1) target length of 20 cm, (2) dissipation of heat deposited by 40 μA of electron beam current and (3) operation without introducing uncorrected false asymmetries at a level $> 5\%$ of the overall uncertainty in the measurement ($\Delta A \approx 10^{-8}$ over the entire run for any individual source of false asymmetry). The modifications required for backward angle running are:

- extension of the target support to longitudinally center the target in the magnet in the backward angle orientation (this extension pipe already exists),
- the port for the target service lines needs to be redesigned to accommodate the space constraints associated with the detector support structure,
- connection of gas panel to D_2 supply tank during LD2 runs.

We are also considering installation of a shorter target cell (10 cm) for backward angle runs to improve separation of elastic and inelastic events.

The liquid hydrogen target cell is connected to a cryogenic loop to recirculate and cool the liquid. The hydrogen will be cooled through heat exchange with compressed helium gas. The liquid hydrogen is thus maintained at 20 K and 25 psia (through connection with the ballast tank). When full, the target cryogenic loop plus target cell and manifold will contain 6.6 liters of liquid hydrogen.

Figure 4.9 is a scale diagram showing the cryotarget centered within the liquid nitrogen shield of the superconducting magnet. The main components of the cryoloop are a pump for circulating the target fluid, a heat exchanger, the target cell, and a manifold to direct

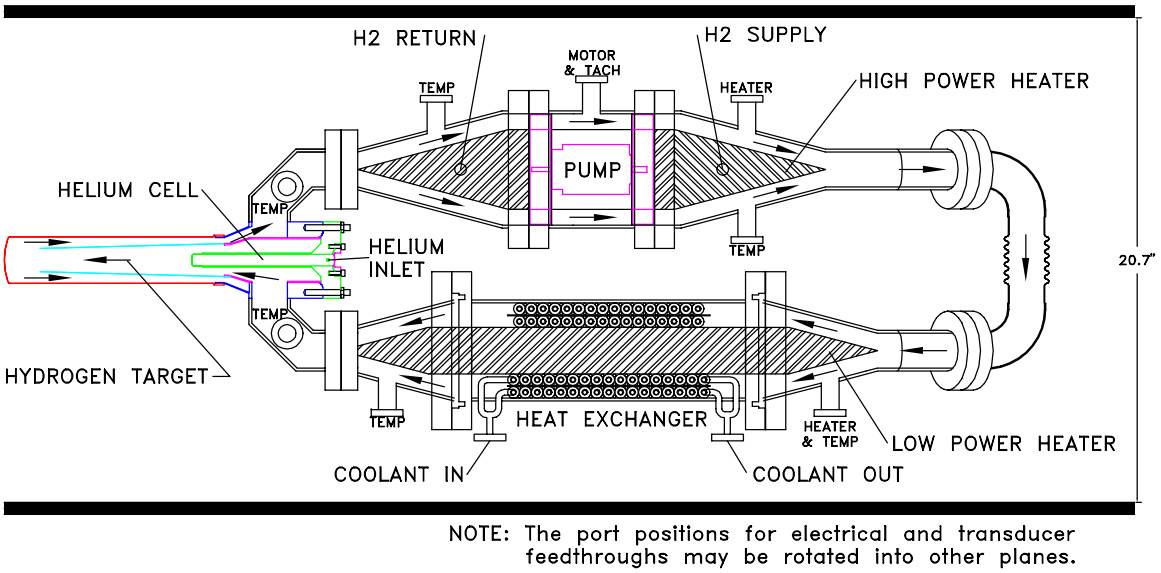

Figure 4.9: Overview of the G0 liquid hydrogen cryotarget. Beam is incident from the right in this view. Exiting scattered electrons of interest emerge at $108^\circ \pm 8^\circ$ with respect to the beam from the hydrogen liquid downstream (left in the figure) of the helium cell.

the fluid flow down the center of the target cell and back near the cell walls. The arrows in the figure indicate the direction of fluid flow everywhere in the loop.

The target cell is fronted by a helium cell which serves three purposes: 1) it effectively extends the entrance of the hydrogen cell beyond the manifold so that exiting particles only traverse hydrogen and thin cell walls, 2) it insures that the exiting particles encounter a region that is symmetric about the beam axis, and 3) it eliminates (to first order) variations in the target thickness with beam position by matching the radius of curvature of the entrance and exit windows of the hydrogen cell. Thus the target−beam interaction region is designed to be axially symmetric and independent of beam position.

Figure 4.10 shows the details of the target cell and manifold. When the pump is running, the liquid hydrogen flows longitudinally in the "beam downstream" direction through the inner flow cone and returns through the annulus between the inner cone and the wall of the hydrogen cell. The distance between the exit window of the helium cell and the exit window of the hydrogen target cell is 20 cm. The holes in the inner cone are essential to prevent collapse of the cone due to Bernoulli pressure; they form an eight-fold symmetric pattern and are aligned with the G0 magnet coils so they are out of the spectrometer acceptance.

The hydrogen target cell consists of a 5 cm diameter tube with a rounded endcap, machined from a solid cylinder of 7075 aluminum. We fabricate the cell by machining the end of the cylinder flat, then pressing it in a form to make the rounded endcap. The radius of curvature of the center of the endcap is 7.6 cm. The outer side wall and endcap are 7.0 ± 0.5 mils thick. To verify that the target cell can withstand the pressure that builds up during

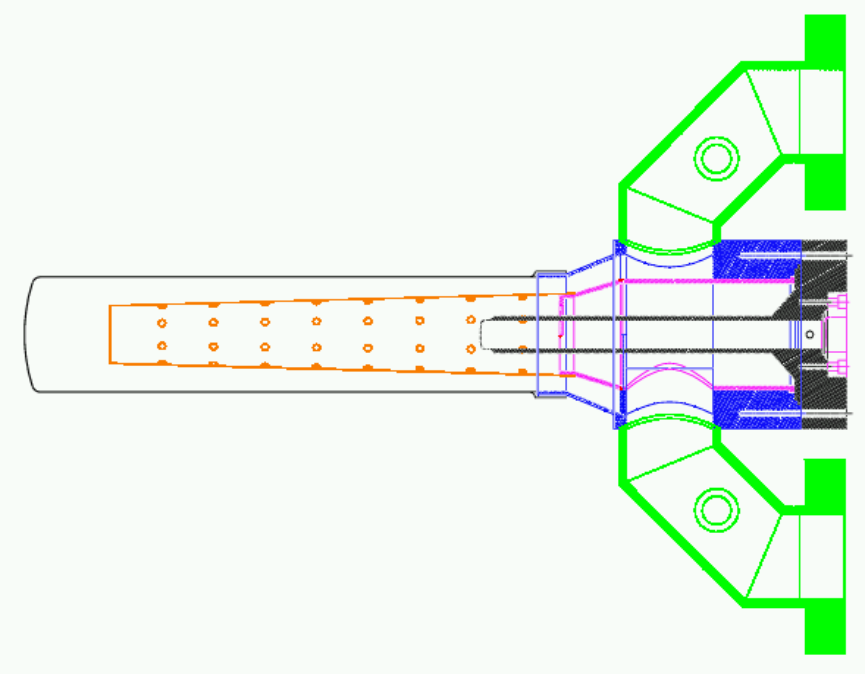

Figure 4.10: Detailed view of the G0 hydrogen target cell, helium cell and manifold. The effective hydrogen target length is 20 cm and the diameter of the outer shell of the target cell is 5 cm. In this view, hydrogen liquid enters in the lower manifold pipe and exits in the upper manifold pipe.

target boiloff, each cell is hydrostatically tested to 100 psid before being soldered to the manifold. This is a factor of 2.4 safety margin over the pressure that we calculate the cell would be subjected to in a catastrophic vacuum failure.

The cryogenic loop contains two heaters, one low power and one high power, to regulate the temperature of the liquid hydrogen. These heaters are identical in function to those used in the Hall C liquid hydrogen target. The high power heater will operate at up to 1000 W maximum power with its main function being to compensate for significant reductions in the beam current. The low power internal heater will be used to make relatively small adjustments to the fluid temperature and will be controlled automatically with a commercial temperature controller in a feedback loop with the temperature sensor on the upstream side of the target cell.

The loop contains a vaneaxial pump capable of displacing 4.8 l/s of liquid hydrogen. This corresponds to a mass flow rate of 333 g/s and gives a velocity in the target region of ~ 7 m/s. The pump motor is inside the cryoloop, similar to the design used in the Hall C cryotargets.

It is important to minimize density fluctuations because they introduce statistical fluctuations into the asymmetry that mask the parity violating asymmetry, requiring a longer running time to achieve the same experimental precision. To reduce resistance and max-

imize the circulating flow rate in the cryogenic loop we have incorporated flow diverter cones at transitions between elements of different diameters.

The G0 target apparatus is presently assembled in the test lab at JLab in preparation for initial cooldown tests (with He only). These tests are expected to commence during June 2001. These tests will include measurements of pump, heat exchanger and heater performance as well as positioning and alignment studies.

4.5 Infrastructure

Since the back-angle configuration has been planned for since the beginning of the G^0 project, many of the infrastructure and installation aspects have already been thought out or implemented. The main change is that the SMS must be moved downstream of the ferris wheel, and the SMS/ferris wheel structure must be rotated 180°. SMS rails to accommodate this configuration change have already been installed in the hall. The ferris wheel platform has been built to accommodate a corresponding (smaller) downstream shift in the ferris wheel location.

At the time of the configuration change, the octants will be removed from the ferris wheel, and the lead/polyboron shielding cylinder will be taken out. It is not needed in the back-angle experiment. Lead shielding will also be removed from the SMS flange. The ferris wheel will be rotated and the octants reinstalled after completion of the FPD/CED reconfiguration. The target service module will mate with the upstream flange of the ferris wheel, moving the target center about 3 m downstream relative to the forward-angle configuration. The details of the SMS turnaround have not been fully worked out yet, however, no substantial problems are foreseen.

New beamline spool pieces will be required. The downstream beam dump shielding will have to be relocated closer to the dump tunnel entrance. Techniques for placing shielding blocks in this location, outside the nominal crane radius, have already been developed and are in use.

The Møller polarimeter will need to be changed to accommodate the lower energies used in this experiment. A similar change was made successfully in the spring 2001 Gen experiment to accommodate Møller measurements at 0.884 GeV by moving the Møller Q1 about 6" upstream. Møller operation at 0.400 GeV will require a further upstream move. Calculations are in progress to quantify this more precisely.

No changes are needed to the cryogenic perimeter transfer lines or U-tubes. No changes to any cable lengths will be required either. Almost all the infrastructure required for the forward-angle portion of G^0 will serve equally well for the backward-angle mode.

5 Management

5.1 Introduction

The G0 experiment will continue to be managed in accordance with the G0 Management Plan which describes the processes and procedures to be used by the Project Manager, the Spokesperson, and the Collaboration to construct, install, and execute the experiment. It includes management organization for both the construction/installation and experiment/physics branches of the project with brief job descriptions for responsible parties. Tracking and reporting of the project status is currently done on a bi-monthly basis. An annual review of the collaboration's progress has been held since 1999 with Barry Barish of Caltech as chair of the review committee.

As described in earlier sections, new physics results dictate that running with a deuterium target will be necessary to complete the G0 program. Also, new understanding of the background rates generated in a deuterium target dictate that additional particle identification will be necessary. The collaboration has been researching these issues and completed considerable work on related simulation, background measurements, detector design, and prototyping. The collaboration's conclusion is that an aerogel Cerenkov detector placed between the FPD and CED scintillator detectors in each octant will provide the best rejection of background. This new detector represents an addition to the G0 project, and as such requires a formal request for a "scope change" which must be approved by the Project Manager, the G0 Spokesperson, the G0 Executive Committee, Larry Cardman, and the funding agency (DOE and NSF) representatives. This change has been informally approved by everyone up to and including the Executive Committee. A formal request to L. Cardman, DOE, and NSF is planned for later this summer. Three collaboration members will take specific responsibility for the Cerenkov project: Charles Davis (TRIUMF) will lead the Canadian effort, Jean-Sebastien Real (Grenoble) will lead the French effort, and Jeff Martin (Caltech) will have overall responsibility for coordinating the Cerenkov project.

5.2 Organization and Funding

As indicated above, the only new piece of equipment (i.e. not included in the existing G0 construction project) required for the backward angle measurements is the set of Cerenkov detectors. Management of the design, construction, installation, and operation of the new Cerenkov detector will be folded into the existing management structure and treated similarly to the backward-angle CED detector project. A detailed plan which includes the significant simulation, design, and prototyping effort at Caltech, as well as the planned construction project at TRIUMF (and possibly France) is currently under discussion. The Canadian group of the G0 collaboration has received an NSERC Major Equipment Grant which will fund half of the development and construction of the eight-

sector aerogel Cerenkov. The funding received is C$90,000 each in the fiscal years 2001 – 2002 and 2002 – 2003, and C$100,000 in the fiscal year 2003-2004. The French groups plan to submit a request for about 1.2M FF in November 2001 (pending the outcomes of this and other reviews). These funds would be available starting at the beginning of calendar 2002.

5.3 Schedule

At present the JLab schedule formally includes only the first half of the commissioning time (23 days) allocated to the experiment. It will occur immediately following the major G0 installation period which begins in February 2002. We expect to finish the forward angle measurement (remaining commissioning time and actual running) in early 2003. We hope this could be followed by commissioning and running of the first Q^2 backward angle points (hydrogen and deuterium together) in early 2004, with the remaining two back angle Q^2 points (again hydrogen and deuterium together) being spread over 2004-5 as laboratory funding allows. Completion of the experiment in 2005 is an important goal of the collaboration and the probability of achieving it will influence the French funding decision.

At the present time, funding for the Cerenkov detectors can be available on a timescale consistent with completion of fabrication and testing of both the Canadian and French components in 2003. In the case of the Canadian project where the final installment will come available in April 2003, purchase of phototubes, for example, could be put off until this time and still allow completion with ample time for testing.

6 Expected Results and Beam Time Request

6.1 Expected Results

This section presents the expected results from the complete program of proposed G^0 running - forward and backward hydrogen measurements and backward deuterium measurements. For the backward measurements, we have investigated the optimum split of time between hydrogen and deuterium running at each momentum transfer point. We show the results of this study in Figure 6.1 for the 0.3 GeV^2 point; the other momentum transfer points show a similar dependence. We conclude that an even split of running time between hydrogen and deuterium is a reasonable compromise. The even split of time for the hydrogen and deuterium running balances the uncertainties in G_E^s and G_M^s (which are minimized with about 60% of the running time on hydrogen) against those in $G_A^e(T=1)$, which are minimized at a small fraction of hydrogen running.

In our error estimates, we assume 700 hours of running time for each of the backward measurements (three on hydrogen and three on deuterium) with a 40 μA beam and 70% polarization. The assumptions we make about the uncertainties in the form factors and other quantities that go into the asymmetry calculation are summarized in Table 6.1. The expected errors on the separated form factors are summarized in Table 6.2. Figure 6.2 shows the overall uncertainties in G_E^s and G_M^s relative to the overall proton form factors G_E^p and G_M^p, and Figure 6.3 shows these uncertainties relative to two representative theoretical calculations. Figure 6.4 shows the uncertainties expected in $G_A^e(T=1)$ relative to the calculation of Zhu, *et al.* [38] where we have extended their $Q^2=0$ calculation by using the standard dipole form for G_A as measured in neutrino scattering. The contribution of the various uncertainties to the total is shown in Tables 6.3-6.5 and Figures 6.5-6.7.

Quantity	Uncertainty
$\Delta G_E^p/G_E^p$	2%
$\Delta G_M^p/G_M^p$	2%
$\Delta G_E^n/G_E^n$	20%
$\Delta G_M^n/G_M^n$	3%
$\Delta P_b/P_b$	2%
$\Delta Q^2/Q^2$	1%
$\Delta G_A^e(T=0)$	.11
ΔR_V^p	.033
ΔR_V^n	.0004

Table 6.1: Uncertainties assumed for the quantities in the asymmetry expression. We note that present JLab experiments 93-026 and 93-038 will improve the precision of G_E^n beyond what is listed here by of order a factor of two.

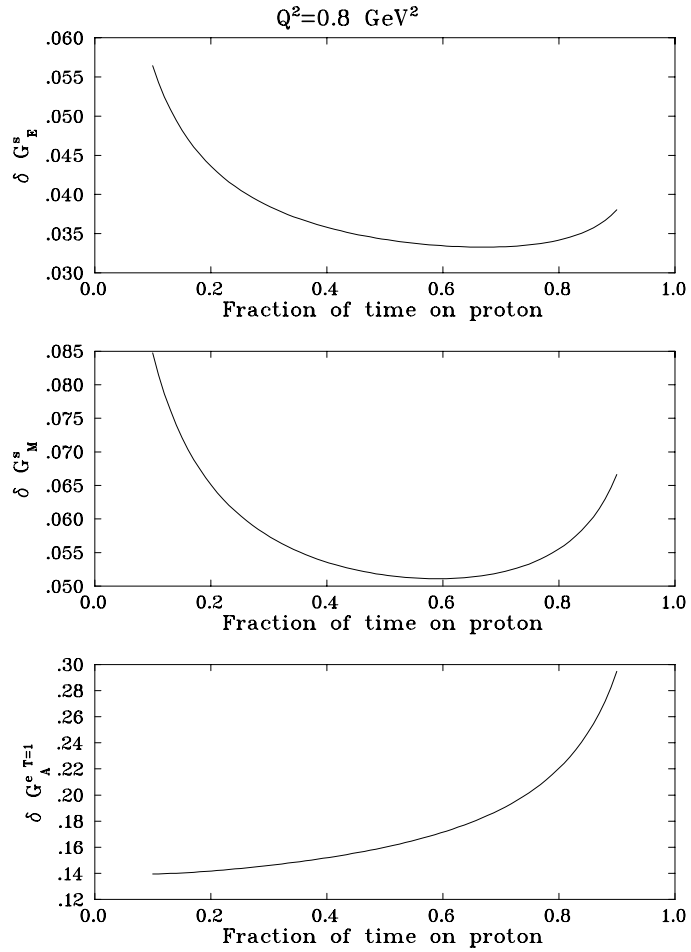

Figure 6.1: Total errors on the separated form factors at $Q^2 = 0.8$ GeV^2 as a function of the fraction of the backward angle running time on hydrogen.

Q^2 (GeV^2)	ΔG_E^s	ΔG_M^s	$\Delta G_A^e(T=1)$
0.3	.031	.112	.222
0.5	.033	.073	.185
0.8	.034	.051	.158

Table 6.2: Expected errors on the separated form factors. These include all statistical and systematic errors.

6.2 Beam Time Request

At this time, we request enough beam time to complete the single backward angle Q^2 measurement at 0.8 GeV^2. For this purpose we request a total of 70 days of beam time. This includes 10 days for commissioning the back angle setup, including the new Cerenkov detectors. The physics production running would then occur with 30 days each for hydrogen and deuterium. This run will require an energy of 0.799 GeV and an average current of

Quantity	0.3 GeV^2	0.5 GeV^2	0.8 GeV^2
A_f	.010	.012	.010
A_b	.019	.020	.024
A_d	.011	.011	.012
G_E^p	.005	.005	.004
G_M^p	.005	.005	.004
G_E^n	.012	.012	.009
G_M^n	.003	.003	.002
Q^2	.007	.008	.008
P_e	.012	.013	.013
$others$	.004	.004	.003
total	.031	.033	.034

Table 6.3: Contributions to the error on G_E^s. The entries for Q^2 and P_e include the errors for all three measurements(f, b, d) added in quadrature. The "others" entry includes $G_A^e(T=0), R_V^p, R_V^n$.

Quantity	0.3 GeV^2	0.5 GeV^2	0.8 GeV^2
A_f	.003	.002	.001
A_b	.078	.049	.036
A_d	.053	.034	.025
G_E^p	.000	.000	.000
G_M^p	.011	.008	.006
G_E^n	.007	.004	.002
G_M^n	.014	.011	.008
Q^2	.028	.019	.012
P_e	.047	.032	.020
$others$	.019	.011	.007
total	.112	.073	.051

Table 6.4: Contributions to the error on G_M^s. The entries for Q^2 and P_e include the errors for all three measurements(f, b, d) added in quadrature. The "others" entry includes $G_A^e(T=0), R_V^p, R_V^n$.

nominally 40 μA with the G^0 pulse structure (one bunch every 32 ns instead of every 2 ns).

Quantity	0.3 GeV^2	0.5 GeV^2	0.8 GeV^2
A_f	.016	.015	.010
A_b	.019	.015	.013
A_d	.170	.139	.127
G_E^p	.023	.011	.005
G_M^p	.015	.018	.016
G_E^n	.022	.016	.010
G_M^n	.043	.033	.023
Q^2	.066	.056	.043
P_e	.111	.096	.076
others	.012	.010	.007
total	.222	.185	.158

Table 6.5: Contributions to the error on $G_A^e(T=1)$. The entries for Q^2 and P_e include the errors for all three measurements(f, b, d) added in quadrature. The "others" entry includes $G_A^e(T=0), R_V^p, R_V^n$.

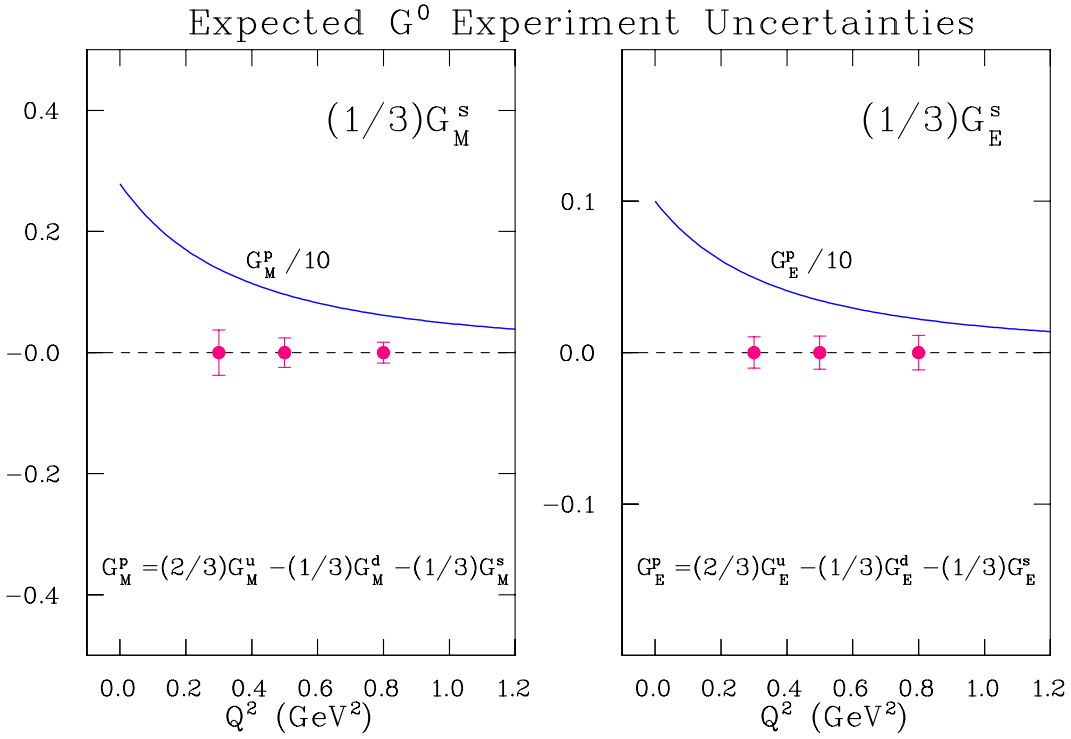

Figure 6.2: Expected errors on the contribution of the strange form factors to the electric and magnetic proton form factors.

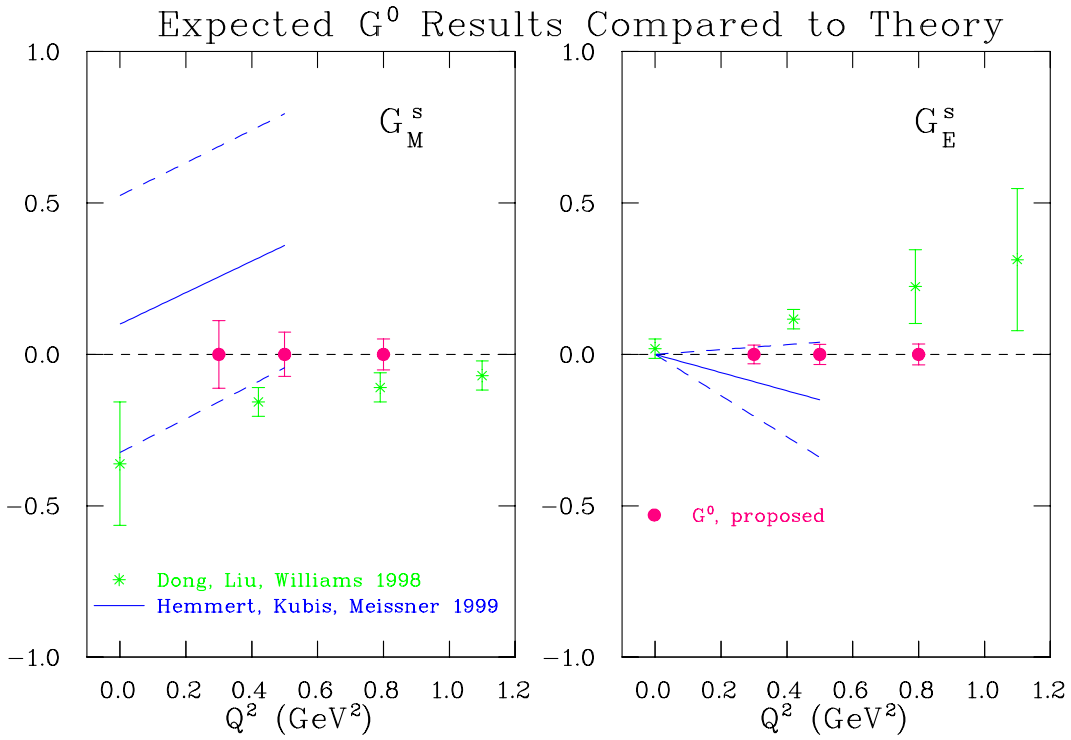

Figure 6.3: Expected G^0 errors compared to a lattice gauge theory prediction (Dong, *et al.*) and a chiral perturbation theory prediction (Hemmert, *et al.*).

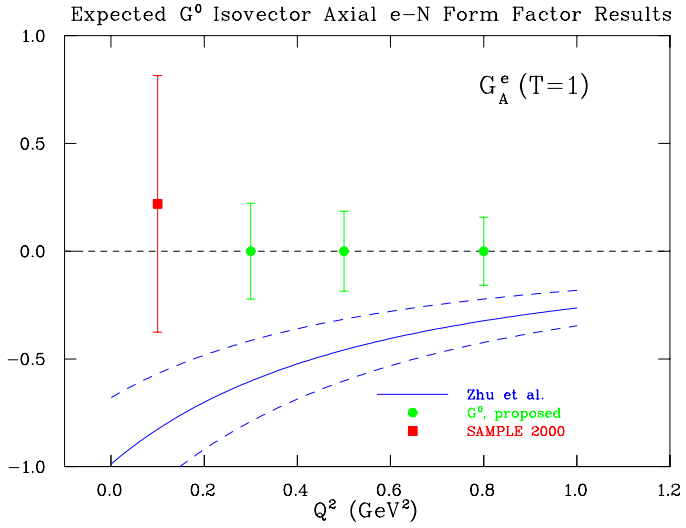

Figure 6.4: Expected errors on the isovector axial e-N form factor. The solid theoretical curve uses the electroweak radiative corrections from Zhu, *et al.* [38] and the dashed curves represent their estimated error in their calculation. We have extended their $Q^2 = 0$ calculation using the standard dipole form for G_A as measured in neutrino scattering.

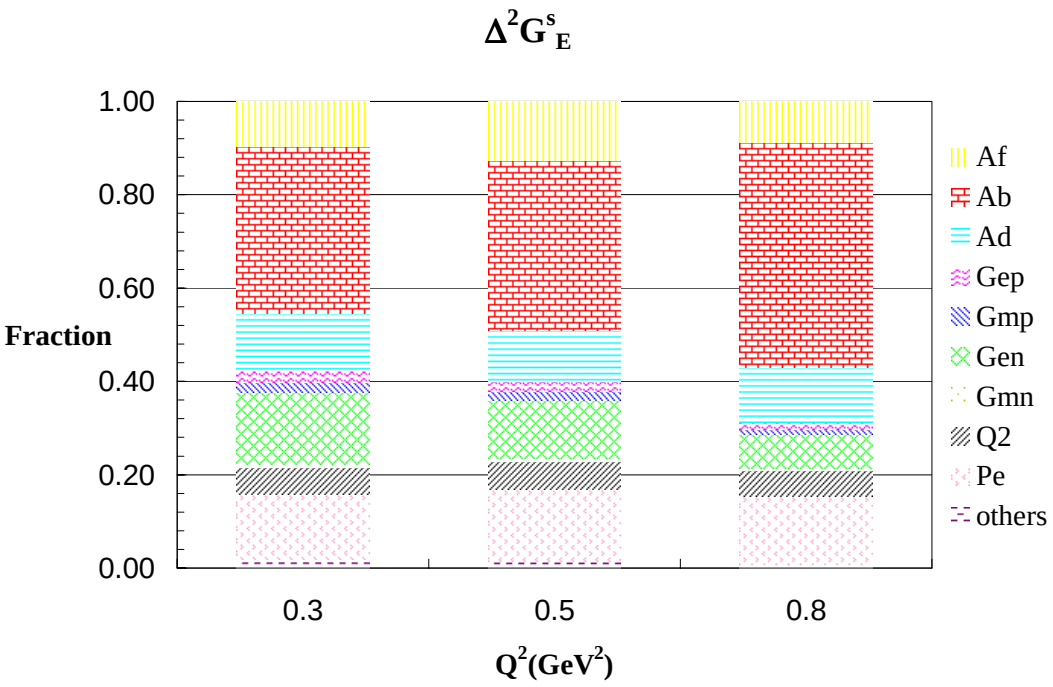

Figure 6.5: Fractional contributions to the error on $\Delta^2 G_E^s$. The entries for Q^2 and P_e include the errors for all three measurements(f, b, d) added in quadrature. The "others" entry includes $G_A^e(T=0), R_V^p, R_V^n$.

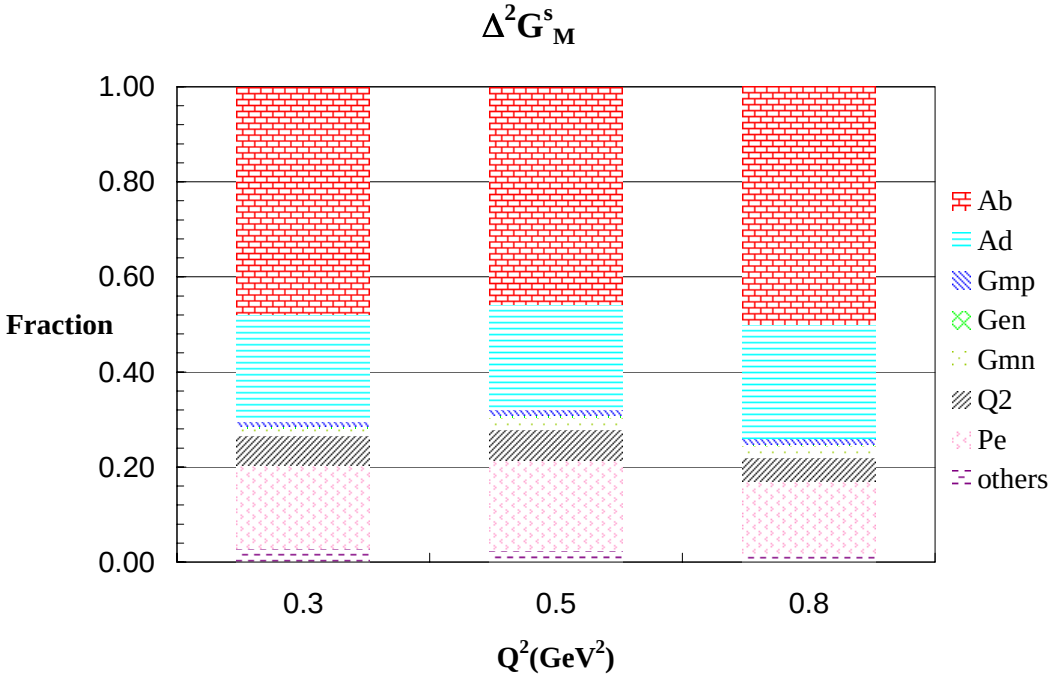

Figure 6.6: Fractional contributions to the error on $\Delta^2 G_M^s$. The entries for Q^2 and P_e include the errors for all three measurements(f, b, d) added in quadrature. The "others" entry includes $G_A^e(T=0), R_V^p, R_V^n$.

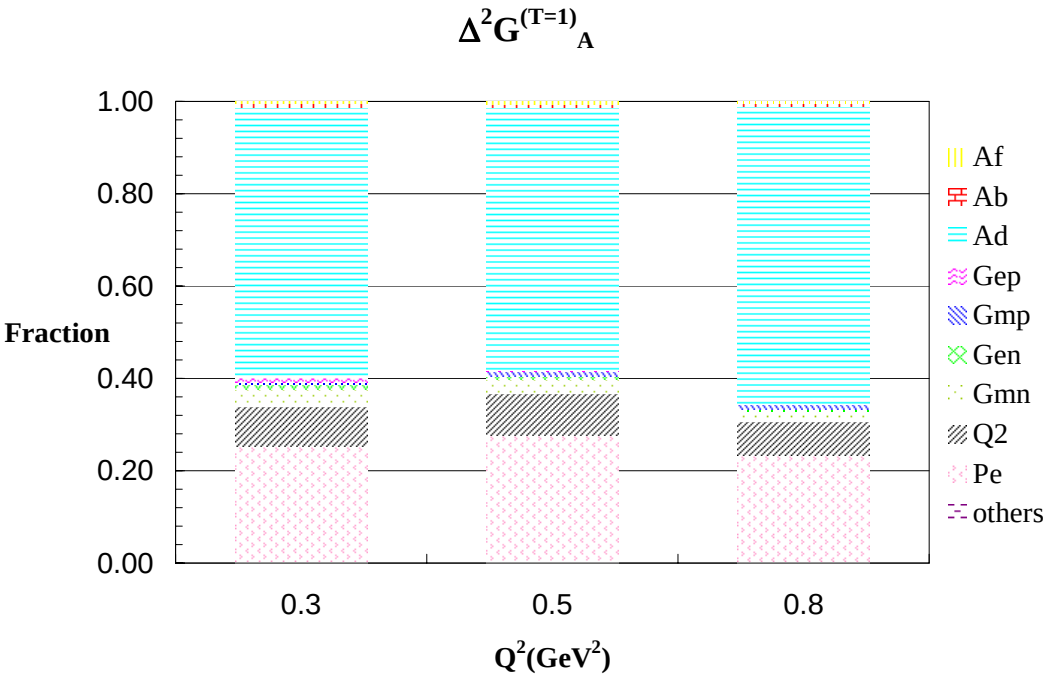

Figure 6.7: Fractional contributions to the error on $\Delta^2 G_A^e(T=1)$. The entries for Q^2 and P_e include the errors for all three measurements(f, b, d) added in quadrature. The "others" entry includes $G_A^e(T=0), R_V^p, R_V^n$.

References

[1] D. H Beck and R. D. McKeown, hep-ph/0102334, to appear in Annual Review of Nuclear and Particle Science.
[2] D. Kaplan and A. Manohar, *Nucl. Phys. B* 310, 527 (1988).
[3] R. D. McKeown, *Phys. Lett.* B219, 140 (1989).
[4] D. H Beck, *Phys. Rev.* D39, 3248 (1989).
[5] M. J. Musolf, *et al.*,, *Phys. Rep.* 239 1 (1994).
[6] M. J. Musolf and B. R. Holstein, *Phys. Lett.* B242, 461 (1990).
[7] E. Hadjimichael, G. I. Poulis, and T. W. Donnelly, Phys. Rev. **C45**, 2666 (1992).
[8] L. Diaconescu, R. Schiavilla, and U. van Kolck, Phys. Rev. **C6304**, 4007 (2001).
[9] M. Ramsey-Musolf, private communication.
[10] Particle Data Group, *Euro. Phys. J.* **C54**, 1 (2000).
[11] G. A. Miller, Phys. Rev. **C57**, 1492 (1998).
[12] W. J. Marciano and A. Sirlin, Phys. Rev. **D27**, 552 (1983); W. J. Marciano and A. Sirlin, Phys. Rev. **D29**, 75 (1984).
[13] M. J. Musolf and M. Burkardt, *Z. Phys.* C61, 433 (1994).
[14] W. Koepf, E. M. Henley, and S. J. Pollock, *Phys. Lett.* B288 11 (1992).
[15] B. R. Holstein in *Proceedings of the Caltech Workshop on Parity Violation in Electron Scattering*, E. J. Beise and R. D. McKeown, Eds., World Scientific, 27 (1990).
[16] H. Ito, *Phys. Rev.* C52, R1750 (1995).
[17] P. Geiger and N. Isgur, Phys. Rev. **D55**, 299 (1997).
[18] L. Hannelius and D.-O. Riska, Phys. Rev. **C62**, 045204 (2000); L. Hannelius, D.-O. Riska, and L.-Y. Glozman, Nucl. Phys. **A665**, 353 (2000).
[19] R. L. Jaffe, *Phys. Lett.* B229, 275 (1989).
[20] H.-W. Hammer, U.-G. Meissner, and D. Drechsel, *Phys. Lett.* B367, 323 (1996).
[21] U.-G. Meissner *et al.*, preprint hep-ph/9701296.
[22] M. J. Musolf, H.-W. Hammer, and D. Drechsel, *Phys. Rev.*. **D55** 2741 (1997).
[23] N. W. Park, J. Schechter, and H. Weigel, *Phys. Rev.* D43, 869 (1991).
[24] S. Hong and B. Park, *Nucl. Phys.* A561, 525 (1993).
[25] C. V. Christov, *et al., Prog. Part. Nucl. Phys.* 37, 1 (1996).
[26] S-T. Hong, B-Y. Park, and D-P. Min, preprint nucl-th/9706008.
[27] S. J. Dong, K. F. Liu, and A. G. Williams, Phys. Rev. D **58**, 074504 (1998).
[28] D. B. Leinweber and A. W. Thomas, Phys. Rev. D **62**, 074505 (2000).
[29] H. Weigel, *et al.*, *Phys. Lett.* B353, 20 (1995).
[30] D. H. Beck and B. R. Holstein, hep-ph0102053, to be published in Int. J. Mod. Phys. E.

[31] S. C. Phatak and Sarira Sahu, *Phys. Lett.* **B321** 11 (1994).
[32] D. Leinweber, *Phys. Rev.* D53, 5115 (1996).
[33] M. J. Ramsey-Musolf and H. Ito, *Phys. Rev.* **C55**, 3066 (1997).
[34] M. J. Musolf, Ph.D. thesis, Princeton University, unpublished.
[35] I. Zel'dovich, JETP Lett. **33**, 1531 (1957).
[36] W. C. Haxton, E. M. Henley, and M. J. Musolf, Phys. Rev. Lett. **63**, 949 (1989); W. Haxton, Science **275**, 1753 (1997).
[37] C. S. Wood *et al.*, Science **275**, 1759 (1997).
[38] S.-L. Zhu, *et al.*, Phys. Rev. **D62**, 033008 (2000).
[39] D.-O. Riska, Nucl. Phys. **A678**, 79 (2000).
[40] C. M. Maekawa and U. van Kolck, Phys. Lett. **B478**, 73 (2000).
[41] C. M. Maekawa, J. S. Viega, and U. van Kolck, Phys. Lett. **B488**, 167 (2000).
[42] B. A. Mueller *et al.*, *Phys. Rev. Lett.* 78, 3824 (1997).
[43] B. A. Mueller, Ph.D. thesis, California Institute of Technology, unpublished.
[44] T. A. Forest, Ph.D. thesis, University of Illinois at Urbana-Champaign, unpublished.
[45] D. P. Spayde, Ph. D. thesis, University of Maryland, unpublished.
[46] D. T. Spayde *et al.*, Phys. Rev. Lett. **84**, 1106 (2000).
[47] R. Hasty, *et al.*, Science **290**, 2117 (2000).
[48] T. R. Hemmert, U.-G. Meissner, and S. Steininger, Phys. Lett. **B437** 184 (1998).
[49] MIT-Bates Lab experiment 00-04, T. Ito, spokesperson.
[50] K.A. Aniol et al. (HAPPEX Collaboration), Phys. Rev. Lett. **82**, 1096 (1999).
[51] K. A. Aniol, et al. (HAPPEX Collaboration), nucl-ex/00060002.
[52] Jefferson Lab experiment 99-115, K. Kumar and D. Lhuillier, spokespersons.
[53] Jefferson Lab experiment 00-003, R. Michaels, P. Souder and R. Urciuoli, spokespersons.
[54] Jefferson Lab experiment 00-114, D. Armstrong, spokesperson.
[55] Jefferson Lab experiment 91-004, E. Beise, spokesperson
[56] Mainz experiment PVA4, D. von Harrach, spokesperson; F. Maas, contact person.
[57] S. Schramm and C. Horowitz, Phys. Rev. **C49**, 2777 (1994).
[58] Kuster and Arenhövel, Nucl Phys. **A626**, 911 (1997).
[59] W.Y.P. Hwang, E.M. Henley, and G.A. Miller, Ann. Phys. **137**, 378 (1981).
[60] B. Desplanque, J.F. Donoghue, and B.R. Holstein, Ann. Phys. **124**, 449 (1980).
[61] S. Pollock, Phys. Rev. **D42**, 3010 (1990).
[62] S. Wells, JLab experiment E97-104.
[63] N. Mukhopadhyay, *et al.*, Nucl. Phys. **A633**, 481 (1998).
[64] P. Amore *et al.*, Los Alamos preprint nucl-ex/0007072.
[65] D. Drechsel, O. Hanstein, S.S. Kamalov and L. Tiator, Nucl. Phys. **A645** (1999) 145.
[66] L. Tiator and L. E. Wright, Nucl. Phys. **A379** (1982) 407.
[67] R. Tieulent and J-S. Réal, *Test of a Photoproduction Generator Using the SOS data of December 1999*, G^0 Technical Report G0-00-019 (July 12, 2000).

[68] J. L. Matthews and R. O. Owens, Nucl. Instrum. Meth. **111** (1973) 157.
[69] J. W. Lightbody Jr. and J. S. O'Connell, Computers in Physics. **May/June** (1988) 57.
[70] R. Tieulent, P. King, A. Lung, J. Martin, M. Pitt, J-S. Réal, J. Roche, Gr. Smith, Gw. Smith, and V. Tadevosyan, *Experimental Background Contributions to the G^0 Backward Angle Measurements*, G^0 Technical Report G0-01-012 (April 21, 2001).
[71] E. Rollinde, *G0GEANT Manual (DRAFT)*, G^0 Technical Report G0-99-035 (June, 1999).
[72] S. P. Wells, N. Simicevic, K. Johnston, and T. A. Forest, and The G^0 Collaboration, *PAC20 Proposal: Measurement of the Parity Violating Asymmetry in the N-¿DELTA Transition (Originally E97-104)*
[73] S.P. Wells, G0-99-008, LATECH-CAPS-99-03b (1999).
[74] C. Murphy, S.P. Wells, and N. Simicevic, G0-99-051, LATECH-CAPS-99-11a (1999).
[75] G. Quéméner and S. Kox, *Aerogel Cerenkov Counter Design for the G0 Spectrometer*, G^0 Technical Report G0-00-052 (December 13, 2000).
[76] J. W. Martin, *Aerogel Cerenkov Counter Design*, G^0 Technical Report G0-00-054 (June 12, 2000).
[77] D. Higinbotham, Nucl. Instrum. and Meth. **A414** (1998) 332.

7 Appendix: Progress Report for 2001 DOE/NSF Progress Review